Journal of the Meteorological Society of Japan (2026) 104:10
https://doi.org/10.1007/s44394-025-00011-2

ARTICLE

Climate simulations using MRI-ESM2 with 60 km resolution atmosphere and data assimilated ocean

Ryo Mizuta[1] · **Hirokazu Endo**[1] · **Hideaki Kawai**[1] · **Seiji Yukimoto**[1] · **Kohei Yoshida**[1] · **Hiromasa Yoshimura**[1] · **Hiroyuki Tsujino**[1] · **Takafumi Miyasaka**[1,2] · **Hiroyuki Murakami**[3] · **Yusuke Ushijima**[4] · **Chiharu Takahashi**[5] · **Masayoshi Ishii**[1]

Received: 4 July 2025 / Accepted: 4 December 2025

Abstract

To explicitly represent short-term atmosphere-ocean interactions while adequately simulating long-term regional-scale climate, climate simulations from the mid-20th century to the present were performed using the Meteorological Research Institute Earth System Model version 2 (MRI-ESM2), with the atmosphere of 60 km horizontal resolution and assimilating ocean observation. A monthly objective analysis of the ocean temperature and salinity were assimilated with a relaxation time of 10 days. Short time-scale atmosphere-ocean interactions, such as precipitation variations that lag behind sea-surface temperature (SST) variations, and SST decreases due to the passage of intense tropical cyclones, are represented in a manner similar to a fully coupled model. In addition, the performance of the model in reproducing climate over long time scales is comparable to our previous atmosphere-only simulations with prescribed observed SSTs, both over the global scale and over East Asia. The overestimation of intense tropical cyclones at mid-latitudes, which was seen in the atmosphere-only simulations, has been improved. The seasonal progression of the East Asian monsoon is also well simulated. These results are expected to contribute to reducing the uncertainty in the assessment of global warming impact, especially for extreme events in the Asian region.

Keywords Climate model · Atmosphere-ocean interaction · Tropical cyclones · Regional climate · Extreme events

1 Introduction

Changes caused by global warming include not only changes in mean climatic conditions, but also changes in the frequency and intensity of extreme events such as heavy precipitation and heat waves (IPCC 2021). The latter have significant impacts on natural disasters, agriculture, water resources, human health, and so on. Along with the recent warming of the mean temperature, changes in extreme events are already being detected using event attribution methods (Stott 2016), not only in temperature but also in precipitation extremes (e.g. Imada et al. 2020).

To accurately evaluate the changes in the frequency and strength of extreme events, long-term climate model simulations over several decades are required at a sufficiently high resolution to represent the events realistically. In addition, because the characteristics of extreme events highly depend on regions and seasons in which the events occur, the global models need to be able to simulate the regional climate with sufficient performance. For instance, the early summer East Asian monsoon is characterized by a narrow rain band that migrates northward with the seasonal progression, often causing extreme precipitation events leading to floods, landslides, and other disasters. To reliably project the changes in the frequency and strength of these events, it is essential to capture the latitude and migration of this

✉ Ryo Mizuta
rmizuta@mri-jma.go.jp

1 Meteorological Research Institute, Japan Meteorological Agency, Tsukuba, Japan

2 Research Center for Advanced Science and Technology, University of Tokyo, Tokyo, Japan

3 Geophysical Fluid Dynamics Laboratory, National Oceanic and Atmospheric Administration, Princeton, USA

4 Center for Marine Environmental Studies, Ehime University, Matsuyama, Japan

5 Atmosphere and Ocean Research Institute, University of Tokyo, Kashiwa, Japan

rain band on sub-monthly time scales. However, accurately capturing these features in coupled models remains challenging. The coupled models consist of many components including the atmosphere, ocean, land surface, aerosols, chemical transport, and the carbon cycle. Due to the insufficient configurations of the complex interactions between these components, simulated sea surface temperature (SST) errors are still large enough to distort the simulation of the location and intensity of severe storms, and to degrade the quality of the representation of extreme precipitation statistics (Wehner et al. 2021). Dynamical downscaling with regional climate models cannot adequately correct such errors in storm locations.

Based on this background, we have been using global atmospheric models with prescribed sea-surface temperature (SST) for future projections of extreme events. The response to future global warming is examined by comparing the simulations with prescribed observed SSTs (AMIP-type simulations) to those with future SST changes in coupled model simulations of the Coupled Models intercomparison Projects (CMIPs) added to the observed SSTs. Using observed SSTs as lower boundary conditions in present-day simulations can avoid the large biases in the coupled models, thereby enabling us to obtain reliable regional climate information (Kitoh et al. 2016). Atmospheric simulations using the above-mentioned SSTs with horizontal resolutions of 60 km–20 km, which is higher than most CMIP6 coupled models (Eyring et al. 2016), have allowed us to examine the changes in precipitation extremes associated with tropical cyclones and Asian summer monsoon rainfall (e.g. Murakami et al. 2012; Endo et al. 2012). The simulation results have also been used for dynamical downscaling around Japan by regional climate models with resolutions of 20 km, 5 km, and 2 km, to investigate small-scale orographic effects governed by mesoscale dynamics and physics (Kawase et al. 2021). Large ensemble simulations have also been performed using a combination of global 60 km and regional 20 km models, which have been published as the Database for Policy Decision-making for Future climate change (d4PDF: Mizuta et al. 2017; Fujita et al. 2019; Nosaka et al. 2020; Ishii and Mori 2020). Using d4PDF, changes in the occurrence probability of rare events, event attribution, and uncertainty of changes due to internal variability in the climate system were examined for intense tropical cyclones (Yoshida et al. 2017), heavy precipitation (Imada et al. 2020), and extreme snowfall events (Kawase et al. 2016). A similar framework of climate simulation has been used in the High Resolution Model Intercomparison Project (HighResMIP; Haarsma et al. 2016) atmospheric model experiment to discuss the model uncertainties from a variety of perspectives (e.g. Roberts et al. 2020; Mizuta et al. 2022).

However, the method of rigidly prescribing SSTs in the atmospheric experiments does not include atmosphere-ocean interactions, such as the ocean stirring effect of tropical cyclones passing over. In this regard, while Murakami et al. (2012) reported that the spatial distribution of intense tropical cyclones in the AMIP-type simulations is biased poleward compared to observations, Ogata et al. (2015) showed that forcing by the observed SST on a time scale of about a week in a coupled model can improve the spatial distribution of intense tropical cyclones, without compromising the other characteristics of the tropical cyclones. Considering that coupled models outperform atmosphere-only models in representing both the climatology and interannual variability of the East Asian summer monsoon (Song and Zhou 2014), models that include atmosphere-ocean interactions are more suitable for climate projection in East Asia.

In this paper, we introduce an earth system model equipped with a high-resolution atmospheric model, in which observed temperatures and salinities are assimilated in the ocean component on a time scale of 10 days. This model is expected to be able to represent both the short-term atmosphere-ocean interactions and the long-term climate closer to observations on global and regional scales. Simulations with the model were performed from the mid-20th century to the present. By comparing the results with simulations without assimilation, we examine how well the short-term atmosphere-ocean interaction is represented. We also examine how well the long-term climate was represented by comparison with atmospheric model simulations. In addition, the simulations with a high-resolution atmosphere are compared with d4PDF, previous high-resolution large-scale ensemble simulations, in terms of how the short-term atmosphere-ocean interactions contribute to the representation of intra-seasonal variability and extreme events associated with the Asian monsoon and tropical cyclones.

2 Data and methods

The Meteorological Research Institute Earth System Model version 2 (MRI-ESM2; Yukimoto et al. 2019; Kawai et al. 2019) is used. This model is one of the models participating in CMIP6, which consists of four component models of atmosphere-land, ocean, aerosol, and atmospheric chemistry. The atmosphere-land component, MRI-AGCM3.5, has a horizontal resolution of TL159 (approximately 120 km) and 80 vertical levels (model top at 0.01 hPa). The ocean component, MRI.COMv4 (Tsujino et al. 2017), has a tripolar grid with a nominal horizontal resolution of 1° in longitude and 0.5° in latitude.

In this paper, the ocean temperature, salinity, and sea ice concentration (SIC) observations are assimilated in the oceanic component during the climate simulations with MRI-ESM2. The observational data used for the temperature and salinity is a monthly objective analysis (Ishii et al. 2017), provided at the top 28 WOA13 levels (Levitus et al. 2015) ranging from the sea surface to 3000 m. The subsurface temperature analysis at the sea surface is equivalent to COBE-SST2 (Hirahara et al. 2014), and the SIC observations are taken from COBE-SST2. The assimilation method used here is Incremental Analysis Update (IAU; Bloom et al. 1996; Huang et al. 2002). A similar method was used in decadal climate projections using earth system models (Tatebe et al. 2012). The differences in temperature and salinity between the daily interpolated monthly analysis and model are computed every day, and their increments, the differences divided by the all integration time steps for 10 days, are added to the corresponding model variables. The ocean observation time used here is 2 days ahead of the model time, instead of the retroactive model integration that is often employed by the IAU. The computed increments are attenuated with increasing water depth, and the increments are set to be zero below 500 m. The sea ice model working in MRI.COMv4 uses five sea-ice categories to represent complex dynamic and thermodynamic processes of sea ice of different thicknesses. The SIC data assimilation is applied to the thinnest thickness category by IAU with the assimilation time scale of 5 days. In this manuscript, the climate simulation using the above ocean data-assimilation is referred to as Temporally Sequential Experiments with Coupled model (TSE-C). Figure S1 shows the standard deviations of SST increments given to the model by the ocean data assimilation, compared with those of daily SST changes in the climate simulation of ESM2_60km. The former is less than 0.1 K/day in most areas, much smaller than the latter. This indicates that model SSTs evolves predominantly according to the model physics and dynamics.

In Sect. 3, we compare the fully coupled ESM2 experiment (ESM2_120km) with the TSE-C experiment (TSE-C_120km) at the atmospheric resolution of 120 km. In addition, an AMIP-type experiment with daily SSTs used in the HighResMIP *highresSST-present* experiment (HadISST2; Kennedy et al. 2017) was also conducted (AMIP_120km). The ESM2_120km experiment is the first ensemble member of the *historical* experiment of MRI-ESM2 published at CMIP6. In TSE-C_120km and AMIP_120km, the resolutions and model parameters of the ESM2 components are the same as in ESM2_120km, except for the ocean assimilation process. In Sect. 4, the atmospheric model resolution is increased from 120 km (TL159) to 60 km (TL319), for the fully coupled experiment (ESM2_60km) and the TSE-C experiment (TSE-C_60km). Since the climate representation of the atmospheric model is resolution dependent, the changes were made to refine the representation of climatology, seasonal progression, etc. in the 60km model, as described in Appendix A. In Sect. 5, we compare the performance of the climate representation in 12 members of the TSE-C_60km ensemble experiment with 12 members of the d4PDF global 60 km experiment. The d4PDF uses the previous version of MRI-AGCM (MRI-AGCM3.2; Mizuta et al. 2012), with the same TL319 horizontal resolution, and is an AMIP-type experiment with monthly SST and sea ice concentration of COBE-SST2. In both experiments, the ensemble consists of climate simulations starting from different initial conditions and providing different perturbations of SST and SIC among members (Mizuta et al. 2017). The above-mentioned experiments are summarized in Table 1, and difference in model configurations for the TSE-C_60km and the d4PDF experiments are listed in Table 2.

The simulated climate is verified with observational datasets and reanalysis datasets. We mainly used JRA-3Q reanalysis (Kosaka et al. 2024), and Global Precipitation Climatology Project (GPCP) monthly (Adler et al. 2003) and pentad (Xie et al. 2011) data with a 2.5° grid spacing, and daily data with a 1° grid spacing (Huffman et al. 2001). In addition, Climate Prediction Center Merged Analysis of Precipitation (CMAP; Xie and Arkin 1997), Integrated Multi-satellite Retrievals for the Global Precipitation Measurement (IMERG; Huffman et al. 2020), ERA5 reanalysis (Hersbach et al. 2023), and COBE-SST2 are also used. For tropical cyclones, "best-track" data for the period 1981–2020 were obtained from the International Best Track

Table 1 List of the experiments

Experiment name	Model	AGCM horizontal resolution	Experiment type	Number of ensemble members	Oceanic forcing
ESM2_120km	MRI-ESM2	120 km	*historical*	1	none
ESM2_60km	MRI-ESM2	60 km	*historical*	1	none
TSE-C_120km	MRI-ESM2	120 km	*historical*	1	data assimilation
TSE-C_60km	MRI-ESM2	60 km	*historical*	12	data assimilation
AMIP_120km	MRI-ESM2	120 km	*amip*	1	prescribed daily SST
d4PDF	MRI-AGCM3.2	60 km	*amip*	12	prescribed monthly SST

Table 2 Difference in model configurations for the TSE-C_60km and the d4PDF experiments

Experiment name	TSE-C_60km	d4PDF
Atmosphere-land	MRI-AGCM3.5 (Yukimoto et al. 2019)	MRI-AGCM3.2 (Mizuta et al. 2012)
Horizontal resolution	60 km	60 km
Vertical levels	80 (top at 0.01 hPa)	64 (top at 0.01 hPa)
Radiation	JMA (2007) modified	JMA (2007)
Cumulus convection	Yoshimura et al. (2015) modified	Yoshimura et al. (2015)
Cloud	Kawai et al. (2019)	Tiedtke (1993)
Planetary boundary layer	Nakanishi (2001), Nakanishi and Niino (2004) level 2	Mellor and Yamada (1974, 1982) level 2
Gravity wave drag	Iwasaki et al. (1989), Hines (1997)	Iwasaki et al. (1989)
Land surface	HAL (Yukimoto et al. 2011)	Hirai et al. (2007)
Ocean	MRI.COMv4 (Tsujino et al. 2017), with assimilating monthly objective analysis	prescribed monthly-mean sea-surface temperature
Aerosol	MASINGAR mk-2r4c (Tanaka et al. 2003; Tanaka and Ogi 2017)	prescribed monthly-mean aerosol density
Atmospheric chemistry	MRI-CCM2.1 (Deushi and Shibata 2011)	prescribed monthly-mean ozone density

Archive for Climate Stewardship (IBTrACS v04r00; Knapp et al. 2010).

3 Verification of atmosphere-ocean interaction

First, we compare the ESM2_120km, TSE-C_120km, and AMIP_120km experiments performed at the same atmosphere resolution, mainly focusing on observed and simulated precipitation.

3.1 SST/precipitation correlations

One of the phenomena that arise from the short-term atmosphere-ocean interaction is the time lag between SST variability and precipitation variability. Higher SSTs locally cause instability in the lower atmosphere. This in turn enhances convective activity, leading to an increase in cloud cover and reduction in downward shortwave radiation. At the same time, the enhanced convective activity increases the upward latent heat flux at the ocean surface due to increased wind speeds, resulting in a gradual decrease in SST. As a result, a phase difference of about five to ten days appears between SST and precipitation variability (Woolnough et al. 2000; Arakawa and Kitoh 2004).

Figure 1 presents the lag regression coefficients of daily SST and surface heat flux components with respect to precipitation over the western North Pacific region (130–150°E, 10–20°N). Observations and the reanalysis show that precipitation has the highest correlation with the SST about 10 days before, and the lowest correlation with the SST about 5 days after (Fig. 1a, b). This indicates that SST reaches a maximum about 10 days before the precipitation maximum and a minimum about 5 days after. The simultaneous correlation of SST and precipitation is negative. In the AMIP_120km experiment (Fig. 1e), precipitation has the highest correlation with the SST 3 about days before, and the simultaneous correlation is positive. In contrast, the ESM2_120km (Fig. 1c) and the TSE-C_120km (Fig. 1d) experiments generally simulate the observed temporal changes, although the regression coefficients are slightly smaller in the TSE-C_120km experiment, likely because the SST is slowly assimilated to the temporal mean.

The lag regressions of the radiative and heat fluxes at the surface are also shown to investigate the factors that cause the SST decrease around the time of precipitation maxima. The reanalysis indicates a substantial contribution from a decrease in downward net shortwave radiation, followed by an increase in latent heat flux to the atmosphere (Fig. 1b). These phenomena are simulated in both ESM2_120km and TSE-C_120km (Fig. 1c, d), although the relationship is slightly weaker in the TSE-C_120km. In the AMIP_120km experiment (Fig. 1e), the flux changes associated with SST increase are reproduced, but the flux is not fed back to the SST.

The spatial distributions of the lags at which the correlation coefficient between precipitation and SST is maximized are shown in Fig. 2. Those for the observations indicate that precipitation have phase lags around 5–10 days behind SST in large part of tropical and subtropical precipitable regions (Fig. 2a), while the lags are mostly within two days for the AMIP_120km experiment (Fig. 2d). Both the TSE-C_120km and ESM2_120km experiments simulate the same level of lag relationship as observed (Fig. 2b, c), except for a slight underestimation over the mid-latitudes of the western North Pacific region. Note that SST has a lag behind precipitation over the extratropics of the Southern Hemisphere in the observation (Fig. 2a). However, the lag is much smaller when using other daily SST datasets (not shown), suggesting this may be a characteristic highly dependent on observational data. Such observational uncertainties could be

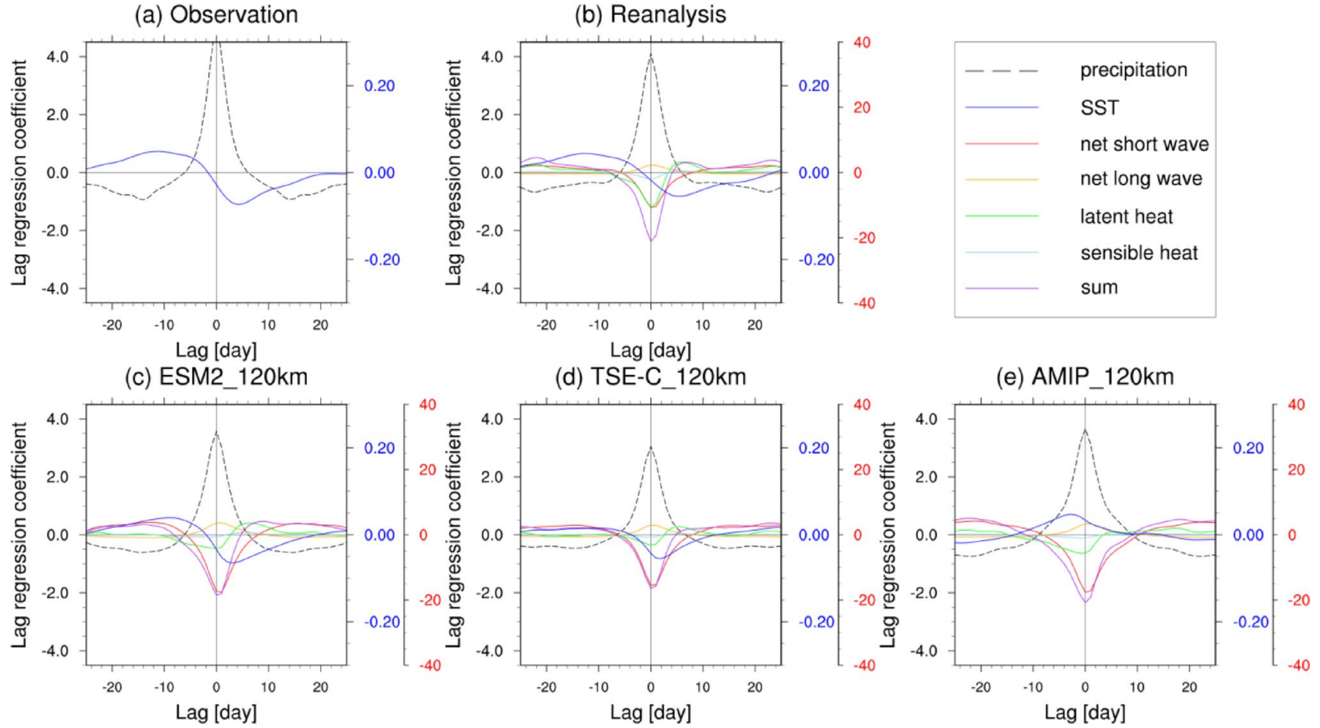

Fig. 1 Lag regression coefficients of SST (right blue axis [K]) and sea surface fluxes (net shortwave, net longwave, latent heat, sensible heat and the sum; right red axis [W/m^2]; downward positive) with respect to precipitation in the western North Pacific (130–150°E, 10–20°N), for (**a**) observation (GPCP and HadISST2), (**b**) JRA-3Q reanalysis, (**c**) ESM2_120km, (**d**) TSE-C_120km and (**e**) AMIP_120km. Dashed lines are lag autoregression coefficients of precipitation (left axis [mm/day]). Each lag regression coefficient is normalized by standard deviation of precipitation variability. Each physical quantity is evaluated based on the regional average of the 100-day high-pass component of the deviation from the daily climatological value. The analysis period is 1997–2014 for the observation and 1981–2010 for the others

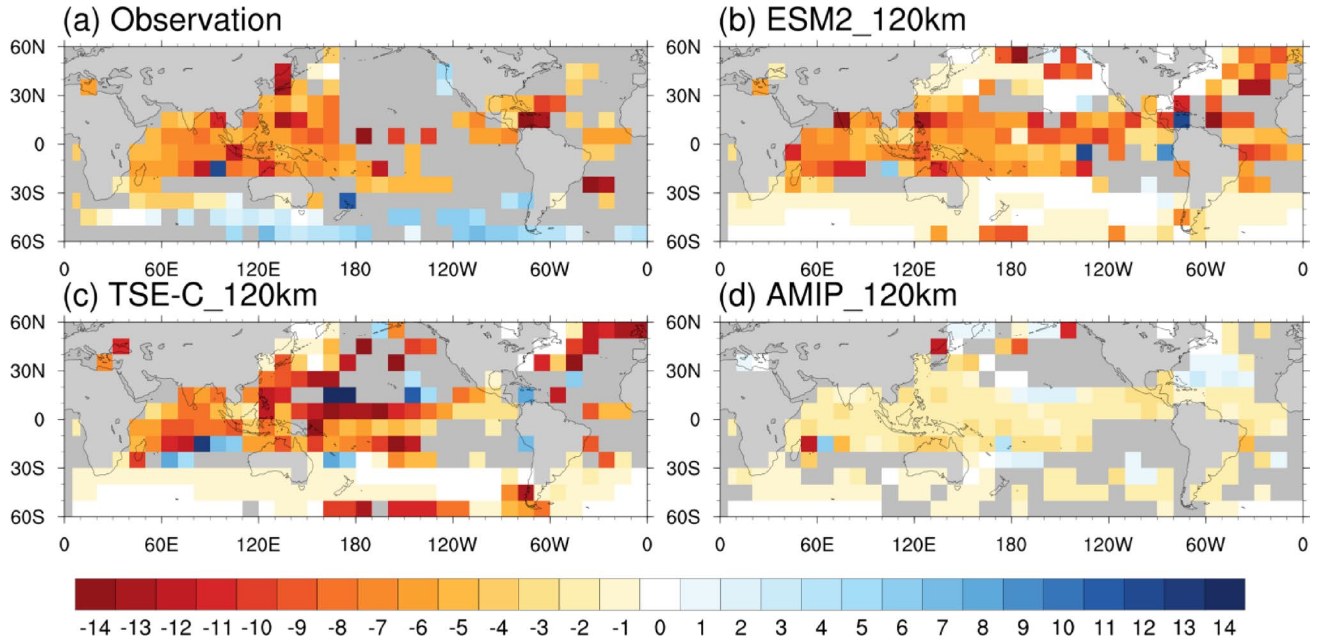

Fig. 2 Lag (in days) when the correlation coefficient between precipitation and SST is highest, for (**a**) the observation (GPCP and HadISST2), (**b**) ESM2_120km, (**c**) TSE-C_120km, and (**d**) AMIP_120km. Negative values indicate SST leads precipitation, and positive values indicate precipitation leads SST. Correlation coefficients are evaluated based on the quantities averaged over each 10° latitude and longitude grid for the 100-day high-pass component of deviations from daily climatology. Only areas with coefficients of 99% significance are presented, and otherwise they are colored gray. The analysis period is the same as in Fig. 1

related to the fact that daily variations are large (Ishii et al. 2025), and satellite observations are sparse due to frequent cloud cover (Reynolds and Chelton 2010) over the area.

Local SST–precipitation correlations on interannual time scales during boreal summer (June–August; JJA) and boreal winter (December–February; DJF) are shown in Fig. 3. The observations (Fig. 3a, e) show positive correlations in many regions, such as the equatorial Pacific, indicating a strong influence of SST on atmospheric convection. By contrast, negative correlations are evident from the western North Pacific to the Bay of Bengal in JJA, and from the Maritime Continent to the SPCZ region in DJF. These features are similarly reproduced in the ESM2_120km experiment (Fig. 3b, f), but not in the AMIP_120km experiment (Fig. 3d, h). The superiority of fully coupled models in reproducing the negative correlations is also apparent in the CMIP6 multi-model simulations (Fig. S2). The limited ability of AMIP-type experiments in capturing the negative SST–precipitation relationship has been widely documented in studies of seasonal prediction (e.g. Wang et al. 2005; Kumar et al. 2013). The observed negative correlations are interpreted in terms of local atmosphere-ocean interactions, such as SST–cloud–radiation feedback and Ekman upwelling associated with strong atmospheric disturbances, as well as atmospheric variability forced by remote SST anomalies (Kumar et al. 2013; Zhou et al. 2018). Note that the latter mechanism can be represented by AGCM experiments, and thus AMIP_120km and CMIP6 AGCMs tend to simulate

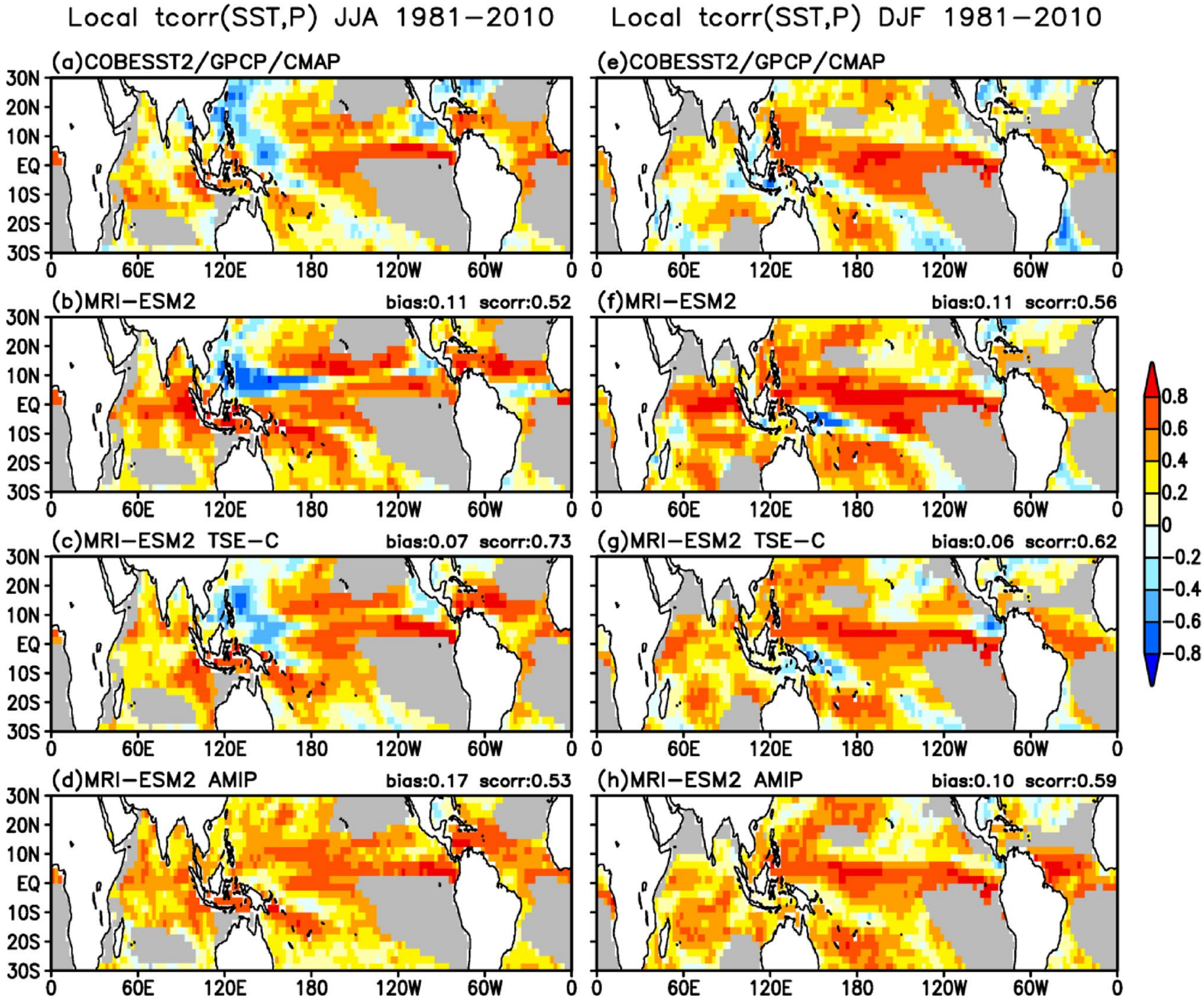

Fig. 3 Local SST–precipitation correlation coefficients for interannual variability during (**a** - **d**) boreal summer (June–August) and (**e** - **h**) boreal winter (December–February), for (**a**, **e**) the observed SST (COBE-SST2) and the average of observation-based precipitation datasets (CMAP and GPCP), (**b**, **f**) ESM2_120km, (**c**, **g**) TSE-C_120km, and (**d**, **h**) AMIP_120km experiments. The analysis period is 1981–2010. Note that tropical-mean SST anomalies were removed before calculating the local anomalies. Numbers in the upper right of each panel indicate bias and spatial pattern correlation coefficient with respect to the observed values. Areas of low precipitation (less than 1 mm/day in the observed climatology) are masked by gray shading

relatively weak correlations over the tropical western North Pacific in JJA (Fig. 3d; Fig. S2c).

The observed negative correlation regions are reproduced in TSE-C_120km, similarly to ESM2_120km (Fig. 3c, g). Spatially averaged difference and spatial correlation coefficient between the simulation and the observations are shown in the upper right of each panel. The TSE-C_120km experiment has the smallest difference and the highest spatial correlation among the three experiments. These high skill scores of TSE-C_120km are likely due to the combination of including atmosphere-ocean interactions and reproducing a realistic SST distribution through assimilation.

3.2 Precipitation climatology

The global-scale seasonal precipitation distributions from observations, the ESM2_120km experiment, the TSE-C_120km experiment, and the AMIP_120km experiment are shown in Fig. 4. The ESM2_120km experiment (Fig. 4b, f) simulates the large-scale features of the observed climatological precipitation reasonably well (Fig. 4a, e), including the Inter-Tropical Convergence Zone (ITCZ) over the Pacific, the Atlantic, and Indian Oceans, the South Pacific Convergence Zone (SPCZ), and monsoon-related precipitation over each continent. However, the SPCZ is zonally oriented in the central Pacific in both seasons, and a spurious ITCZ appears in the southeastern Pacific during DJF (Fig. 4f). This double-ITCZ bias is still found in many coupled models (Tian and Dong 2020; Si et al. 2021). In addition, precipitation around India during JJA is underestimated (Fig. 4b). These are alleviated by prescribing observed SSTs in AMIP_120km (Fig. 4d, h), indicating that the seasonal precipitation distribution is strongly influenced by the SST distribution. The precipitation distribution in TSE-C_120km (Fig. 4c, g) is comparable to that in AMIP_120km, reflecting that SSTs in TSE-C_120km are very close to observation on the seasonal-mean time scale (Figure S3). Biases, root mean square errors (RMSEs), and spatial correlation coefficient with respect to the observations are shown in the upper right of each panel. While the biases do not differ significantly among the three experiments, RMSE and spatial correlation coefficients of TSE-C_120km are substantially better than those of ESM2_120km, and they are comparable to those of AGCM_120km.

4 Performance of the high-resolution atmosphere

In this section, we discuss the representation of long-term climate and atmosphere-ocean interaction when the atmospheric model is increased from 120 km to 60 km.

4.1 Zonal-mean temperature and wind

Differences of the zonal-mean temperature of ESM2_120km, TSE-C_120km, and TSE-C_60km from JRA-3Q reanalysis data in JJA and DJF are compared in Fig. 5. In both seasons, the temperature is about 2 K lower than the reanalysis in the middle to upper troposphere at mid-latitudes in the ESM2_120km experiment (Fig. 5a, d). In contrast, the bias is smaller in the TSE-C_120km experiment, especially in the middle troposphere (Fig. 5b, e). This fact indicates that a large part of the tropospheric temperature biases can be attributed to the SST biases in ESM2_120km. Although the SST biases in MRI-ESM2 were significantly reduced from the previous earth system model, a low SST bias remains in the mid-latitudes in ESM2_120km (Yukimoto et al. 2019). The low temperature biases in the mid-latitude troposphere in the TSE-C_60km experiment are even smaller than in TSE-C_120km, especially in the Southern Hemisphere (Fig. 5c, f). In addition, high temperature biases over 2 K, which are commonly found in the lower stratosphere, become smaller in TSE-C_60km.

Figure 6 shows the differences in zonal-mean zonal wind from the reanalysis. In the ESM2_120km experiment, the positive/negative biases are seen on the equatorward/poleward side of the subtropical jets in both seasons in both hemispheres (Fig. 6a, d), indicating the jets are shifted equatorward. The shift is more pronounced in the winter hemisphere. These biases are related to the mid-tropospheric temperature difference between the tropics and mid-latitudes (Fig. 5a, d); a larger meridional temperature gradient tends to strengthen the subtropical jet and cause it to shift southward. Such shifts become much smaller in TSE-C_120 km (Fig. 6b, e), especially in the Northern Hemisphere summer, and even smaller in TSE-C_60km (Fig. 6c, f). These are consistent with the reduction of the biases in the meridional temperature gradient (Fig. 5).

It should be noted that the improvements in TSE-C_60km from TSE-C_120 km found in Figs. 5 and 6 are not simply due to the increase in horizontal resolution, but also due to the changes in the Appendix A. An experiment that only increased the horizontal resolution showed little improvements in temperature bias in the middle troposphere temperature and in the subtropical jets (not shown). Changes made in the 60 km model that reduced the low-temperature bias in the mid-latitude middle troposphere has led to the jet improvement.

4.2 SST cooling by tropical cyclones

Strong wind stresses on the sea surface induced by overpassing tropical cyclones (TCs) rapidly stir the ocean vertically through shear-induced vertical mixing and Ekman

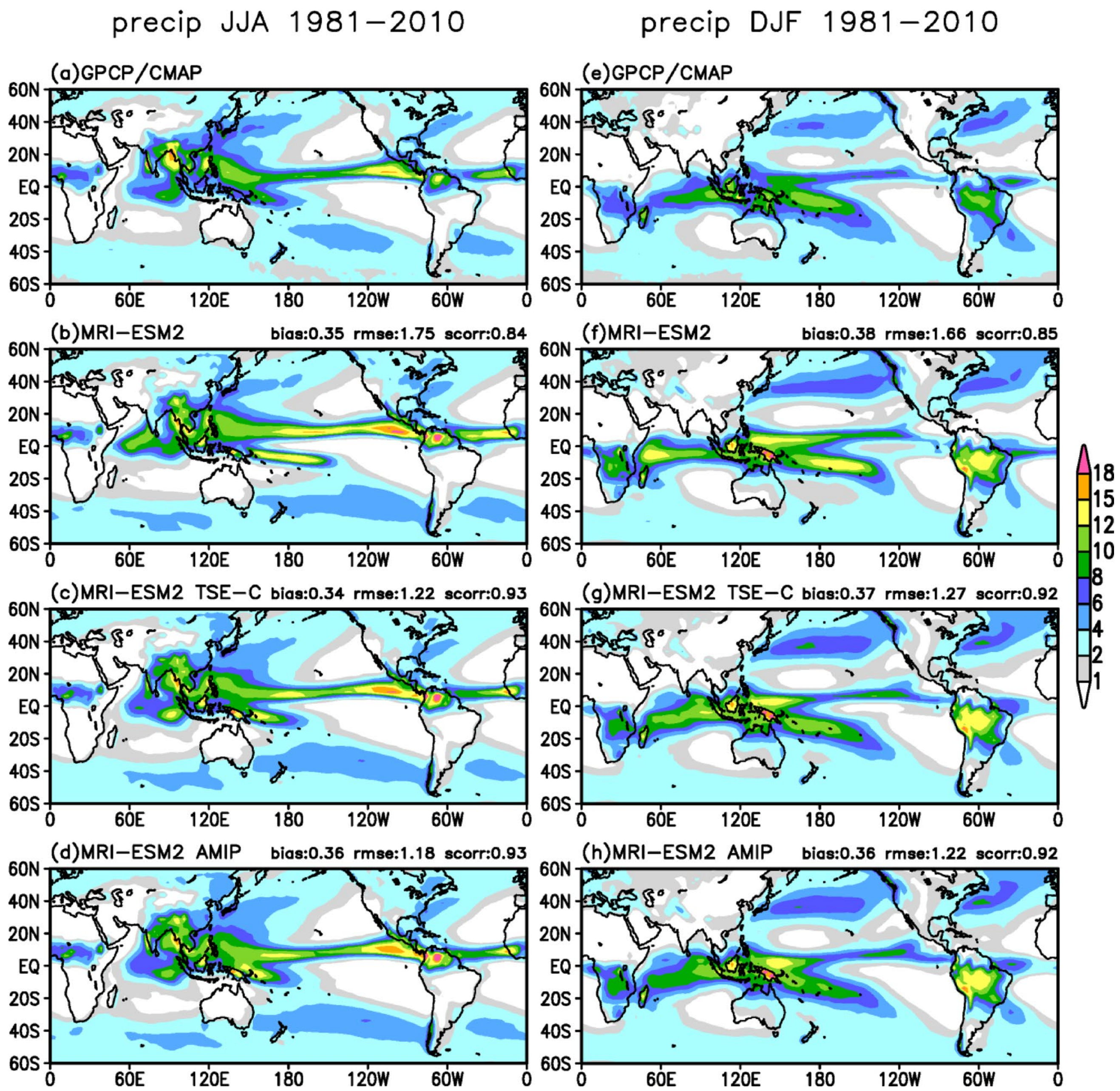

Fig. 4 Spatial distribution of climatological precipitation (mm/day) during (**a** - **d**) JJA and (**e** - **h**) DJF, for (**a**, **e**) the average of observation-based dataset (CMAP and GPCP), (**b**, **f**) ESM2_120km, (**c**, **g**) TSE-C_120km, and (**d**, **h**) AMIP_120km. The numbers in the upper right of each panel are bias, RMSE, and spatial correlation coefficient with respect to the observed values. The analysis period is 1981–2010. Model outputs are re-gridded to the same 2.5° latitude-longitude grid as the observation

upwelling. As latent heat from the warm ocean surface is the primary energy source for TCs, SST cooling due to the ocean stirring weakens TC intensity (e.g. Price 2009; Vincent et al. 2012). Here we assess how these effects are represented in TSE-C_60km and ESM2_60km.

Figure 7 shows the statistics of SST changes from the previous day at the TC center in the western North Pacific. There are many cases of large SST cooling north of 20°N in ESM2_60km (Fig. 7a). The average decrease of these is about 0.4–0.6 K between 120°E and 180°E, and the magnitudes vary in latitude (Fig. 7b). This latitudinal dependence is thought to be related to the thermal structure of the ocean interior such as the ocean mixed layer depth and the water temperature just below the ocean mixed layer. Figure 7c presents the dependence of SST cooling on TC intensity and migration speed. It is evident that slower and stronger TCs exhibit more pronounced SST cooling. These features are also well represented in the TSE-C_60km experiment,

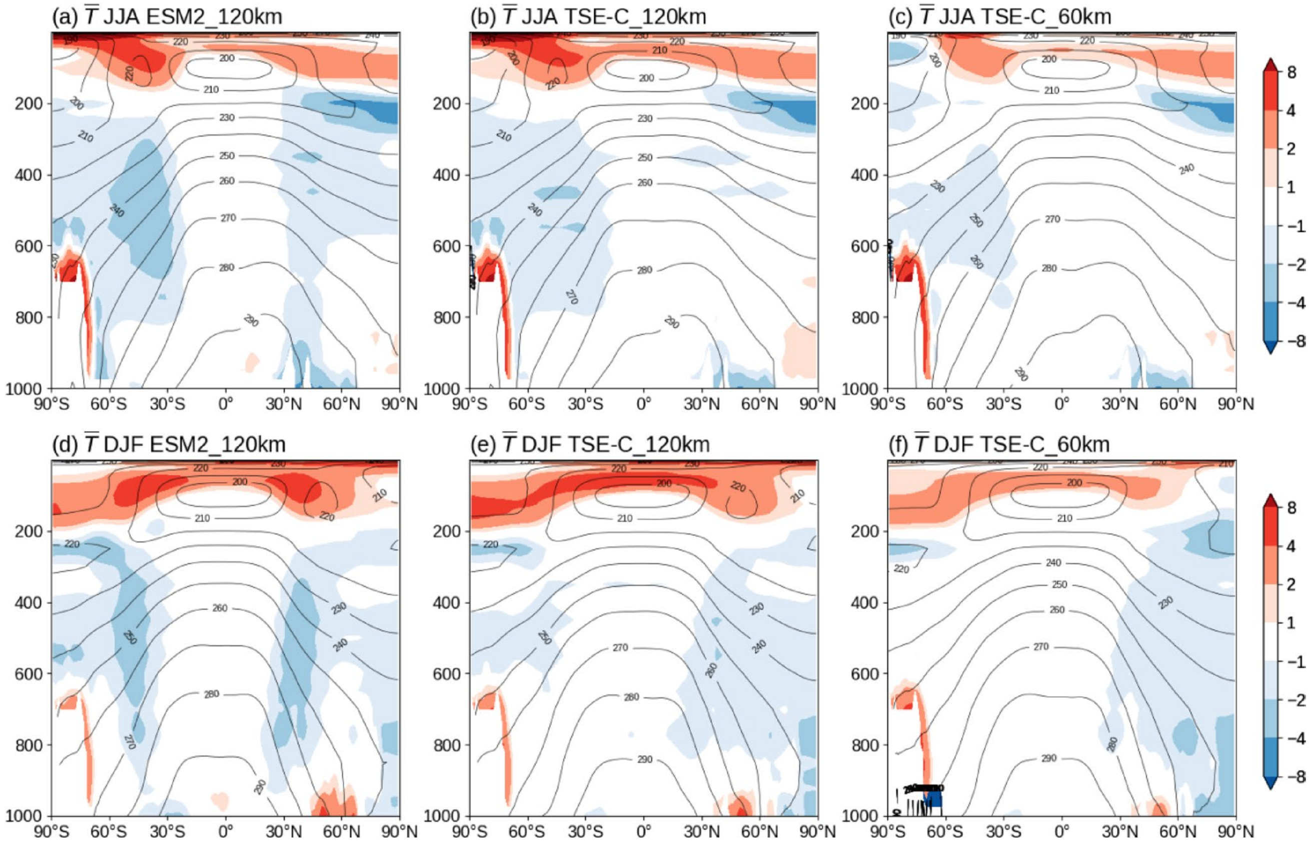

Fig. 5 Zonal-mean temperature (contour) and its anomaly [K] from JRA-3Q reanalysis (shading), during (**a** - **c**) JJA and (**d** - **f**) DJF, for (**a**, **d**) ESM2_120 km, (**b**, **e**) TSE-C_120 km, and (**c**, **f**) TSE-C_60 km experiments. The analysis period is 1981–2010

as shown in Fig. 7d-f. Comparing the magnitude of the SST cooling (Fig. 7b) with that of ESM2_60 km (Fig. 7e), the SST cooling at 20–30°N is slightly weaker. This may be explained as a result of the abrupt change in water temperature being damped by ocean assimilation, although the increment added by the assimilation process is sufficiently small compared to the change in water temperature, as shown in Figure S1.

5 Comparison with d4PDF

In this section, we examine the long-term climate, intra-seasonal variability, and extreme events in the TSE-C_60km experiment, mainly through comparison with the d4PDF experiment.

5.1 Taylor skill scores

The climatological states in the experiments are evaluated using the Taylor skill scores (Taylor 2001). Figure 8 presents the skill scores, defined by Eq. (5) in Taylor (2001), for key meteorological variables: surface air temperature (SAT), precipitation, sea-level pressure (SLP), geopotential height at 500 hPa, zonal and meridional winds at 200 hPa and 850 hPa, and temperature and specific humidity at 850 hPa. The scores for TSE-C_60km are compared with those of d4PDF and the CMIP6 models: 41 models of the *historical* experiment and 47 models of the *amip* experiment.

The skill scores for all variables of TSE-C_60km are comparable to those for the best-performing models among the CMIP6 experiments, for both the global domain (Fig. 8a-c) and East Asia (Fig. 8d-f), except for precipitation over East Asia in DJF. Similar results are found when comparing the scores with the HighResMIP models (Figure S4), suggesting that the skill scores for TSE-C_60km cannot be explained only by the difference in the model resolution. Compared with d4PDF, the skill scores for SAT and SLP in TSE-C_60km are similar, while those for precipitation are slightly lower. For the other variables, the scores are generally similar, although the preponderance varies depending on the variable.

The difference between the TSE-C_60km and d4PDF is caused by not only the incorporation of atmosphere-ocean interactions, but also the revisions of the model configurations, as shown in Table 2. As the skill scores are sensitive to physical parameterizations, more detailed interpretation would likely require a large number of

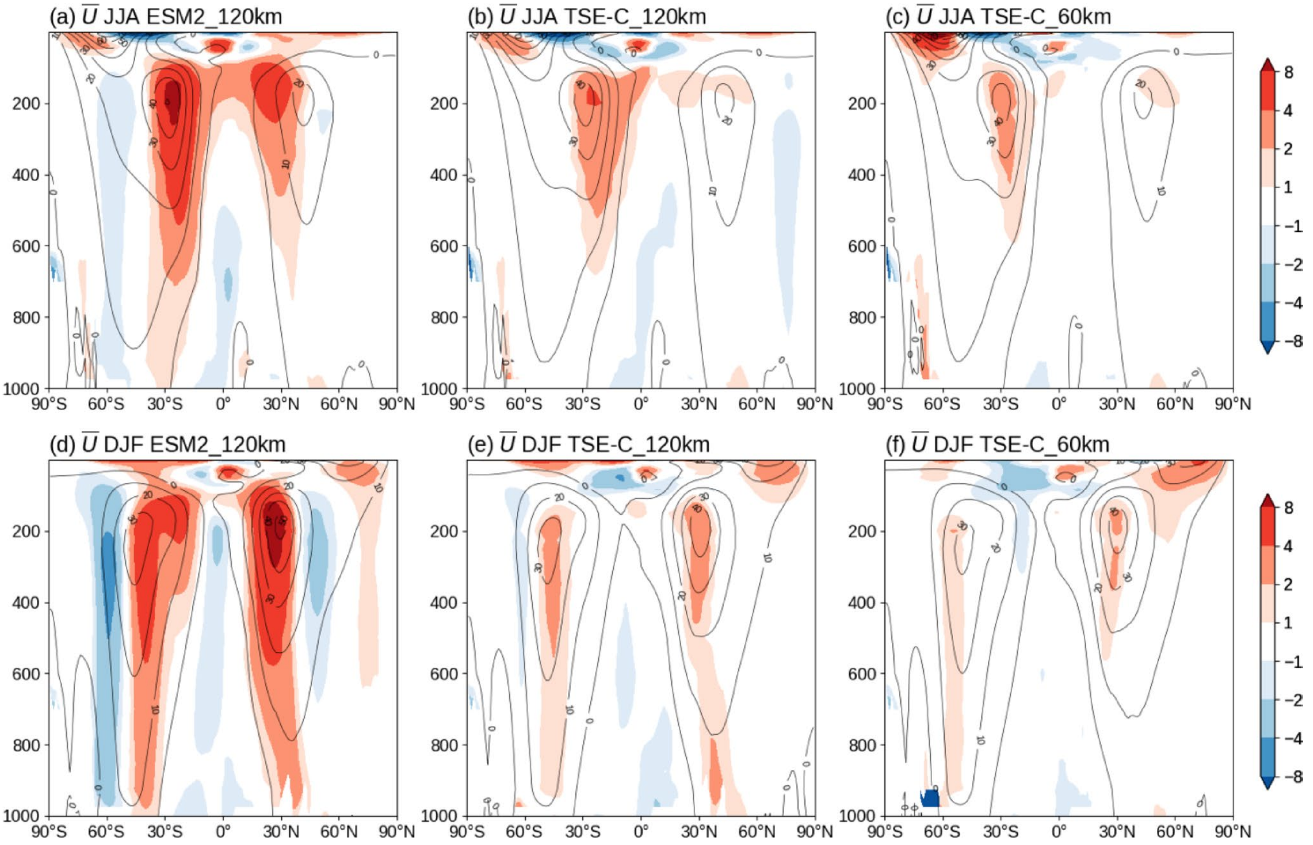

Fig. 6 Same as Fig. 5, but for zonal wind [m/s]

systematic experiments. Regarding the incorporation of atmospheric-ocean interactions, Fig. 4 shows that the long-term mean climate values do not differ significantly between AMIP_120km and TSE-C_120km, suggesting that this is a minor factor. However, to generally assess the effect, we compare the CMIP6 *historical* and *amip* experiments. Globally (Fig. 8a-c), the *amip* experiments generally have higher skill scores than the *historical* experiments, indicating that model skill is affected by the climatological SST bias in the coupled model. In East Asia, in contrast, more variables show higher skill scores in the *historical* experiment than in the *amip* experiment. This is particularly true in summer (Fig. 8f) and is also seen in the annual mean (Fig. 8d). These suggest that the atmosphere-ocean interaction plays an important role in East Asia during the summer season, and may explain the improved scores on several variables in TSE-C_60km in the East Asian region.

5.2 East Asian summer monsoon

The East Asian summer climate is characterized by two rainy periods separated by a break spell. Typically, the northward migration of the Meiyu-Baiu rain band appears in early summer, followed by the break spell that also propagates northward. The second rainy period resumes in late summer or early autumn (Chen et al. 2004; Ding 2007). Heavy precipitation events tend to occur during the two rainy periods, often leading to severe disasters such as floods and landslides, while heat waves typically occur during the break spell. This distinct seasonal cycle is driven by the development of the western Pacific subtropical high and the northward/southward migration of the upper-level East Asian jet, which are integral components of the Asian monsoon system (Wang et al. 2008; Sampe and Xie 2010; Chiang et al. 2020).

The monthly distributions of precipitation, SLP, and 200-hPa zonal winds over East Asia from June to September are shown in Fig. 9. Satellite observations of precipitation show that the Meiyu-Baiu rain band extends from southern China to southern Japan in June (Fig. 9a, b) with a precipitation maximum over southern Kyushu (130°E, 32°N), and it moves northward to the Korean peninsula in July (Fig. 9e, f). Similar migration of precipitation maximum is well represented in both TSE-C_60km and d4PDF (Fig. 9d, h). The peak of the 200 hPa westerly jet, over 30 m/s at 36°N in June, moves northward to 40°N and weakens to about 20 m/s in July. Such seasonal evolution is also well simulated in TSE-C_60km as well as in d4PDF. The climatological

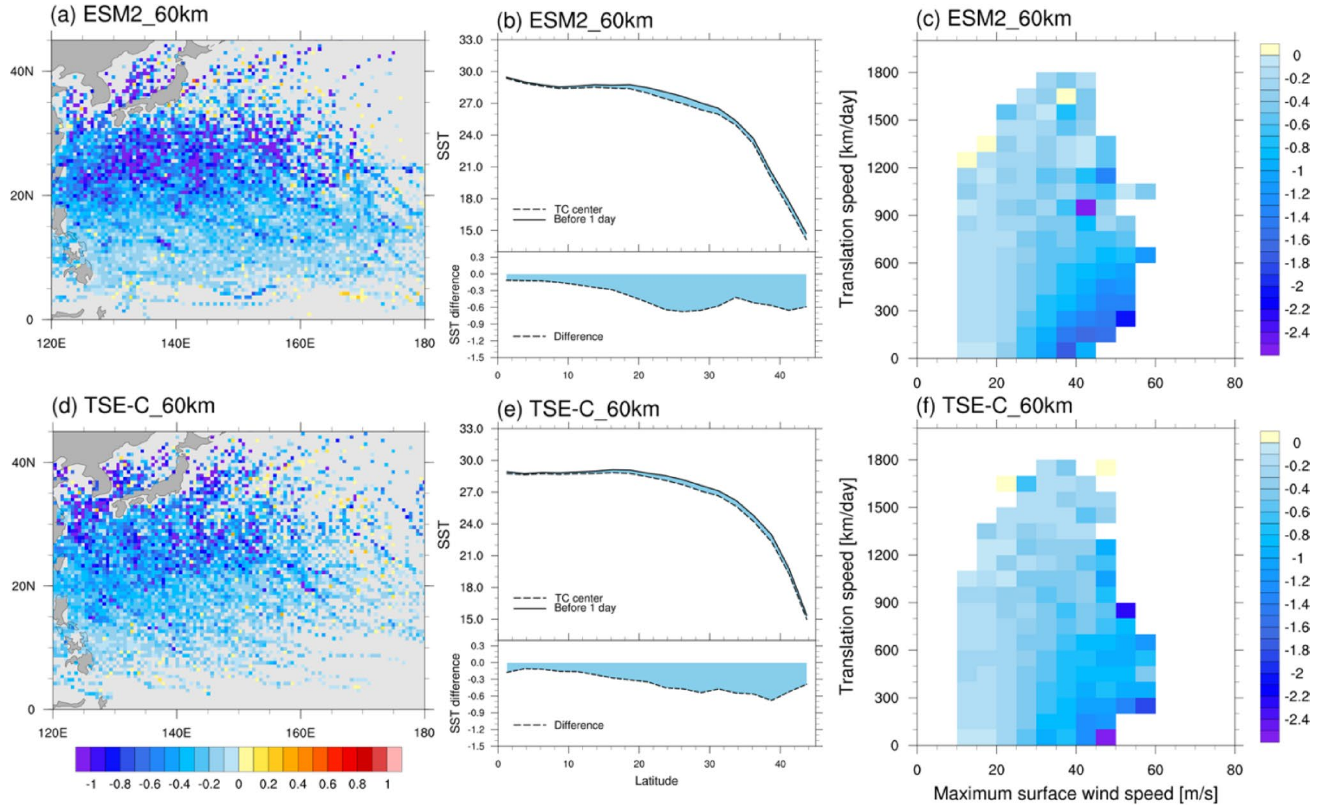

Fig. 7 (**a**, **d**) SST changes from the previous day at the TC center [K/day], (b, e) SST at the TC center on the day of cyclone passage (dashed line) and on the previous day (solid line) in the upper panel, and the changes from the previous day in the lower panel, averaged from 120°E to 180°E, and (**c**, **f**) dependence of the SST change on maximum surface wind speed [m/s] (horizontal axis) and migration speed [km/day] (vertical axis) in the western North Pacific (120–180°E, 0–45°N), for (a-c) ESM2_60km and (d-f) TSE-C_60km. The analysis period is 1981–2010

patterns are also well simulated in August, when the jet shifts further north and precipitation decreases in the southeasterly wind field (Fig. 9i-l). In September, when the jet moves southward, precipitation increases again over Japan (Fig. 9m-p).

Figure 10 illustrates the seasonal progression of precipitation around Japan. The observations show that precipitation caused by the frontal rain bands takes maximum values from late May to mid-July, minimum values from late July to mid-August, and secondary maxima around September (Fig. 10a, b). The TSE-C_60km experiment (Fig. 10c) successfully simulates as observed, and the contrast between the first maximum and the subsequent minimum is more clearly represented than in d4PDF (Fig. 10d). This improvement is possibly associated with the reduction in the zonal wind biases around the upper-level Asian jet. While the Asian jet is located slightly equatorward in July and August in d4PDF (Fig. 9h, l), it is well simulated in TSE-C_60km (Fig. 9g, k). This may be due to the increased precipitation on the continental side of South Asia in TSE-C_60km compared to d4PDF, which likely shifts the Asian jet to higher latitudes by the enhanced upper-level South Asian anticyclone.

While the northward migration of the precipitation maximum latitude is slightly slower in d4PDF than observed (Fig. 10d), TSE-C_60km simulates the migration more realistically (Fig. 10c). However, the weakening of the precipitation in July occurs slightly earlier than observed. In addition, the precipitation amount at the first maximum is slightly lower than in the observations. A previous study by Kusunoki (2018) has noted that the early summer rain band tends to intensify with increasing resolution, suggesting that even higher model resolution may be a solution for more consistent precipitation with observations.

5.3 Tropical cyclones

As shown in Fig. 7, the SST cooling due to the stirring effect of passing TCs is represented in TSE-C_60km. Here, the climatological distribution of TCs is examined. Figure 11a-c compares the TC tracks from TSE-C_60km from 1981 to 2020 with those of d4PDF and the observational dataset. The model-simulated TCs are extracted using the TC extraction tool (Murakami et al. 2012). To ensure that the global occurrence counts are consistent with observations,

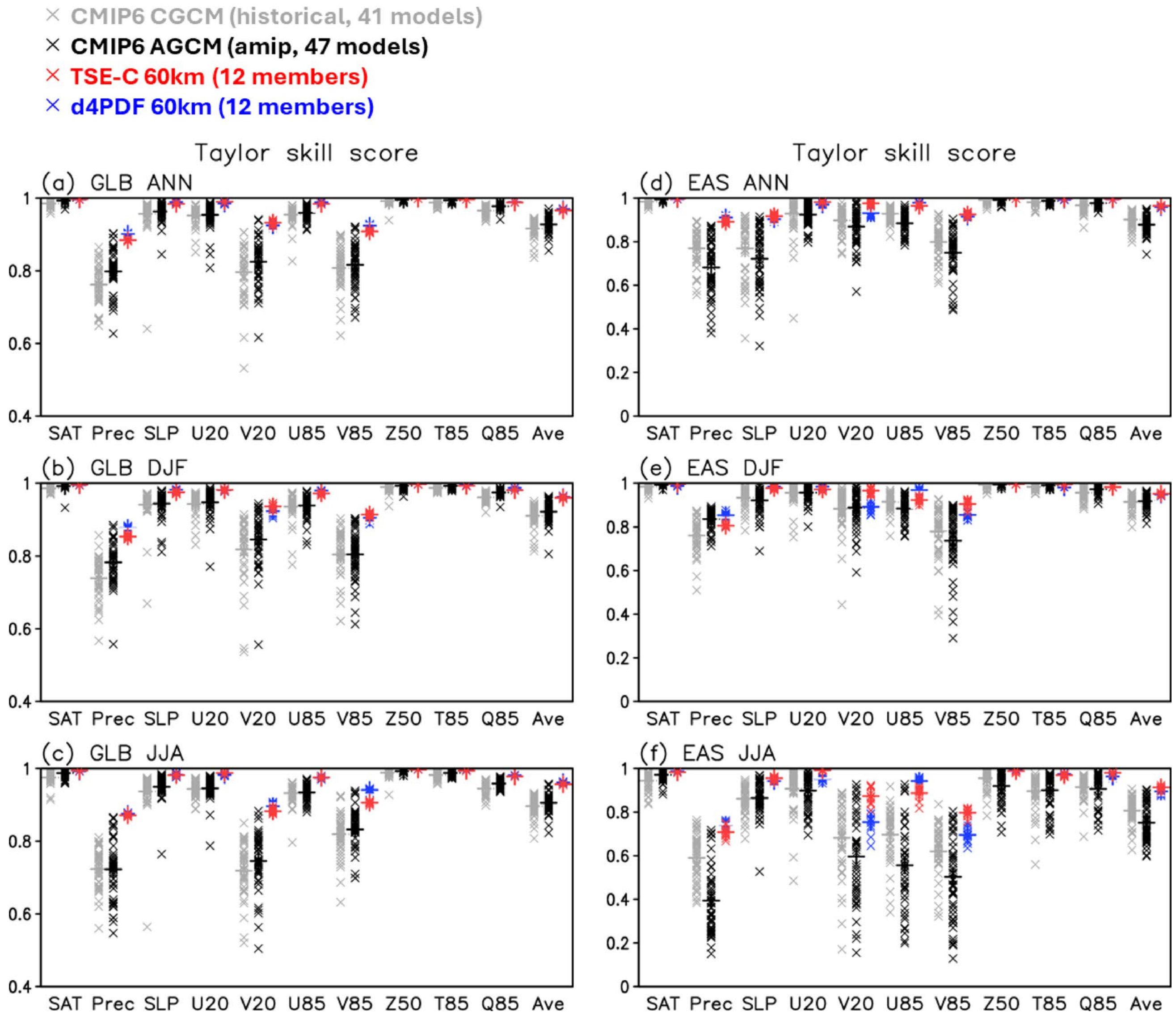

Fig. 8 Taylor skill scores for climatological distributions for (**a** - **c**) the global domain and (**d** - **f**) East Asia (100–160°E, 20–50°N), for (**a**, **d**) annual mean, (**b**, **e**) DJF, and (**c**, **f**) JJA. The scores of TSE-C_60km (12 members; red) are compared with those of d4PDF (12 members; blue), CMIP6 CGCM *historical* experiments (41 models; gray), and CMIP6 AGCM *amip* experiments (47 models; black). Evaluated variables include surface air temperature (SAT), precipitation (Prec), sea-level pressure (SLP), zonal and meridional winds at 200 hPa (U20, V20) and 850 hPa (U85, V85), geopotential height at 500 hPa (Z50), temperature and specific humidity at 850 hPa (T85, Q85), and their average score (Ave). Horizontal bars indicate ensemble means. The skill score is defined by Eq. (5) of Taylor (2001). Reference data are the average of CMAP and GPCP for Prec, and JRA-3Q for the other variables. Scores are calculated after re-gridding model outputs to the same 2.5×2.5° grid as the reference data. For SLP and SAT, grid points at elevations above 1000 m are excluded from the calculation to minimize the influence of model topography differences. The analysis period is 1981–2010

the extraction parameters such as 850-hPa maximum wind intensity, 850-hPa relative vorticity, and warm core threshold were adjusted separately for d4PDF and TSE-C_60km. Although the model does not represent wind speeds that fall into categories 4 and 5 due to the insufficient horizontal resolution (60 km), the distribution of the occurrence frequency is well reproduced in d4PDF (Fig. 11b), as shown in Yoshida et al. (2017), and also in TSE-C_60km (Fig. 11c). Looking at the number of occurrences per ocean basin (white numbers in Fig. 11a-c), TSE-C_60km shows an improvement in the number of TC occurrences in the North Atlantic, North Indian Ocean, and Northeast Pacific, compared to d4PDF, while the number of TC occurrences in the Southern Indian Ocean tends to be too high.

However, it is still unclear what caused the differences in TC climatology, particularly the enhanced TC frequency in the South Indian Ocean, between TSE-C_60km and d4PDF. We tested the impact of including the atmospheric-ocean

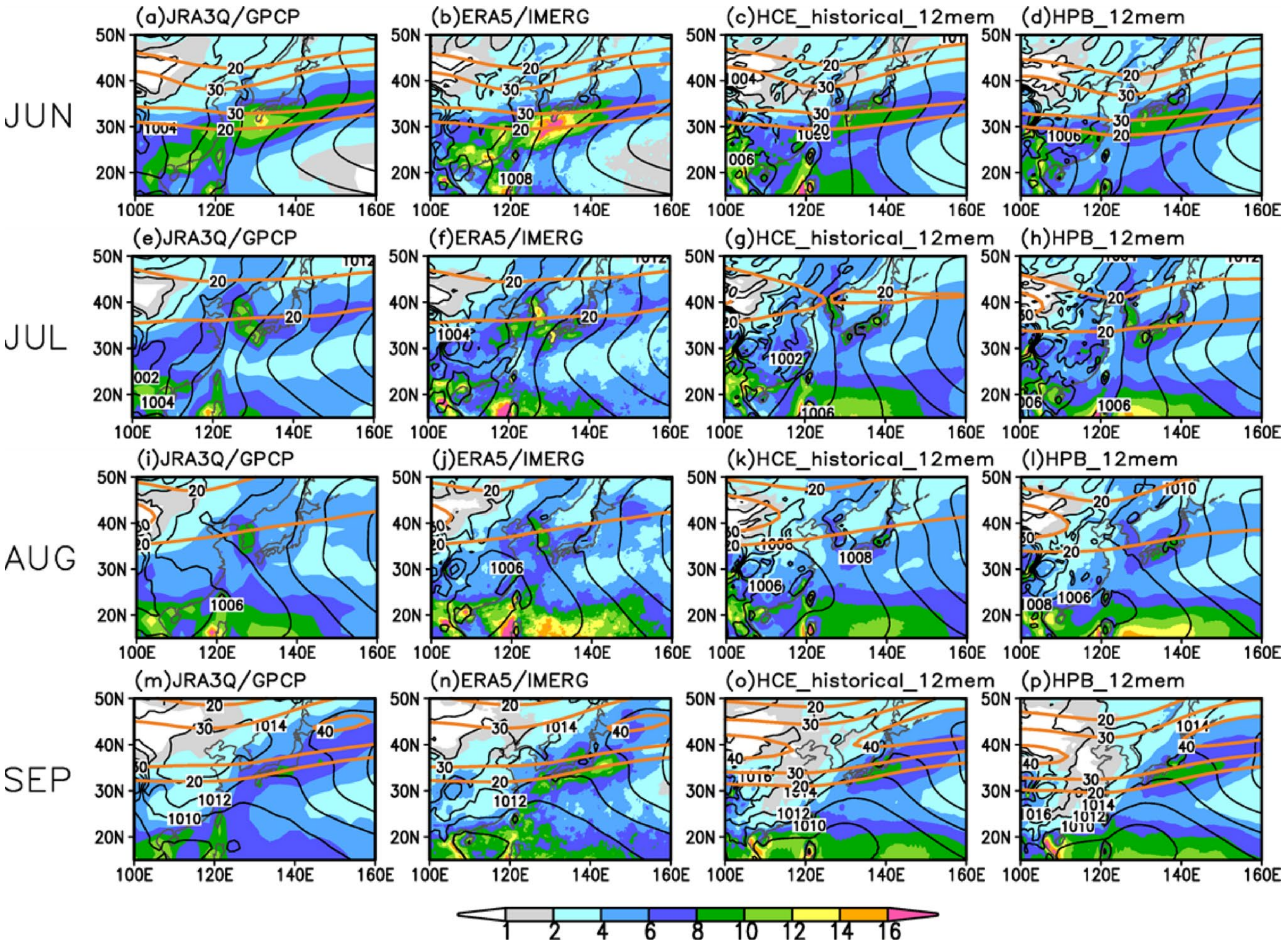

Fig. 9 Monthly-mean precipitation (shading; mm/day), sea-level pressure (black contours; hPa), and 200-hPa zonal wind (orange contours; m/s), for (**a** - **d**) June, (**e** - **h**) July, (**i** - **l**) August and (**m** - **p**) September, for (**a**, **e**, **i**, **m**) reanalysis data (JRA-3Q) and satellite-based observations (GPCP), (**b**, **f**, **j**, **n**) reanalysis data (ERA5) and satellite-based observations (IMERG), (**c**, **g**, **k**, **o**) TSE-C_60km, and (**d**, **h**, **l**, **p**) d4PDF. The analysis period is 2001–2020 for IMERG and 1981–2010 for the other datasets

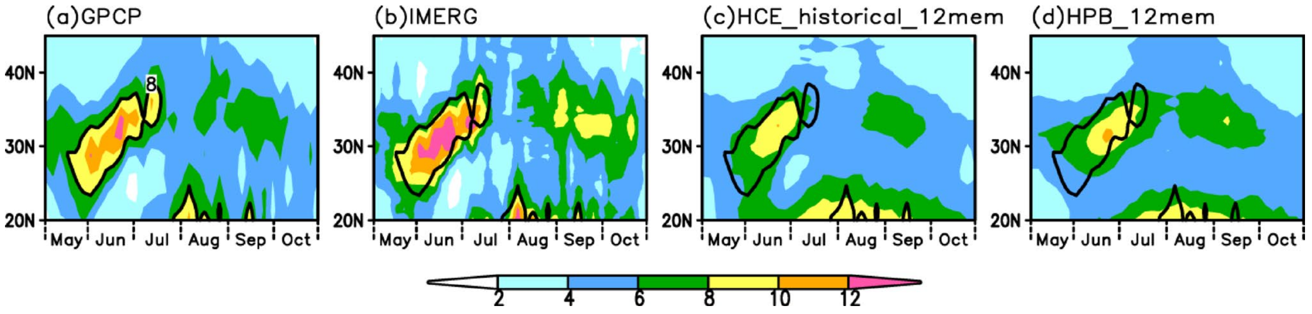

Fig. 10 Latitude-time sections of 3-pentad running-mean precipitation averaged over 125–145°E, for (**a**) GPCP, (**b**) IMERG, (**c**) TSE-C_60km, and (**d**) d4PDF. In each panel, the 8 mm/day contour from GPCP is indicated by a bold black line. The analysis period is the same as in Fig. 9

interactions by 60 km AMIP-type experiment using MRI-ESM2, but found minimal influence on TC climatology except for the intense TCs. Although another possibility is differences in large-scale dynamical and thermodynamical background climatology, such as vertical wind shear and lower-tropospheric relative humidity, our preliminary assessment suggests that differences in large-scale climatology alone cannot fully explain these TC differences. Therefore, we speculate that differences in TC responses to given large-scale conditions (Vecchi et al. 2019; Murakami et al. 2025) play a critical role. However, it remains unclear which specific model configuration changes led to these

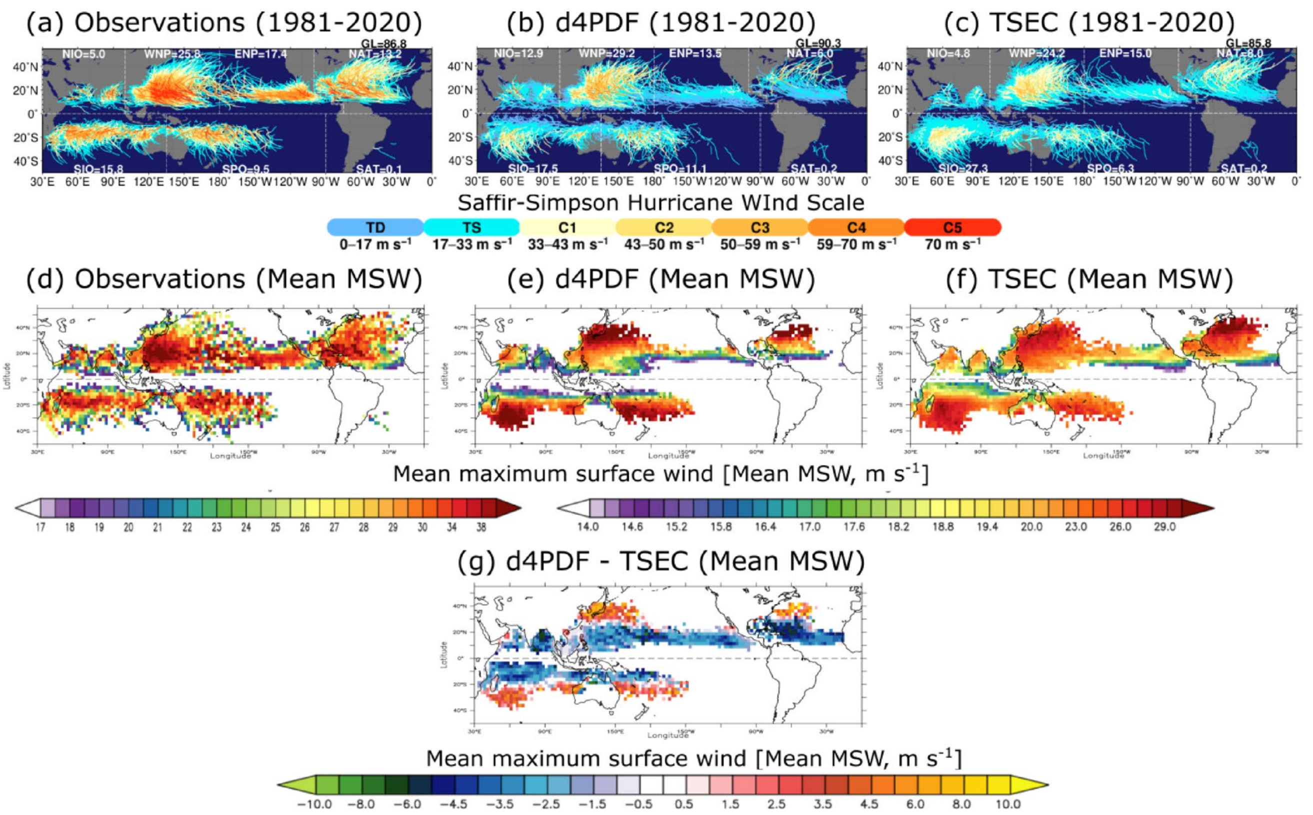

Fig. 11 Global distribution of TC tracks and mean maximum surface wind speed (MSW, m s^{-1}) for (**a**, **d**) IBTrACS best track data, (**b**, **e**) d4PDF, and (**c**, **f**) TSE-C_60km from 1981 to 2020. The numbers in (**a** - **c**) indicate the annual mean number of TCs for each basin. TC tracks in (**a** - **c**) are colored according to their intensities based on the Saffir-Simpson Hurricane Scale. Mean MSW in (**d** - **f**) represents the average TC intensity within each 2.5 × 2.5° grid cell. Only grids with a sample size of five or more TCs are plotted in (**d** - **f**). Panel (**g**) displays the difference between d4PDF and TSE-C_60km. Only a single ensemble member is considered in (**b**, **c**), whereas the 12 ensemble members are considered for (**d** - **g**)

differences. Further investigation will be required to clarify the causes of the differences in TC climatology.

Figure 11d-g shows the distribution of maximum wind speeds of TCs averaged over a 2.5° grid. The observations show that the maximum wind speed is concentrated around the latitudinal bands centered at 20°N and 20°S (Fig. 11d). By contrast, d4PDF shows a shift to 30–35° latitude, indicating that the maximum wind speed is overestimated in the mid-latitudes (Fig. 11e). This overestimation has already been reported by Murakami et al. (2012): the occurrence frequency of intense TCs was overestimated in the mid-latitudes in the 20 km version of the same model as d4PDF. Positive biases in mid-latitude TC intensities are significantly reduced in the TSE-C_60km experiment (Fig. 11g). This is in agreement with Ogata et al. (2015), who reported that the meridional distribution of intense TCs was improved by using the coupled model with forcing the observed SST on a time scale of about a week. Note that TC intensity in TSE-C_60km is still underestimated at low latitudes, probably because the rapid development of TCs in the early stages is not sufficiently simulated due to the lack of horizontal resolution of the atmosphere.

Figure 12 shows the linear trend in the frequency of TC occurrence from 1981 to 2020. Consistent with Murakami et al. (2020), the observations show significant increases in TC frequency in the North Atlantic and North Indian Ocean, and significant decreases in the western Pacific, eastern North Pacific, and South Indian Ocean (Fig. 12a). The TSE-C_60km and d4PDF experiments mostly simulate the observed features in the North Atlantic and the western Pacific (Fig. 12b, c). In addition, TSE-C_60km simulates the observed increase in the North Indian Ocean and the decrease in the eastern Pacific, which are not represented in d4PDF.

While the monthly mean distribution of aerosols was given as an external boundary condition to the atmospheric model in d4PDF, the atmospheric and aerosol models are coupled interactively in the TSE-C model. The fact that the effects of the aerosol trend are now properly reflected is probably related to the improvement of the TC trend. Moreover, the improved trend pattern in TSE-C_60km may also be attributed to its more realistic representation of the relative contributions of different anthropogenic forcings. Recent findings by Wang et al. (2023) suggest that

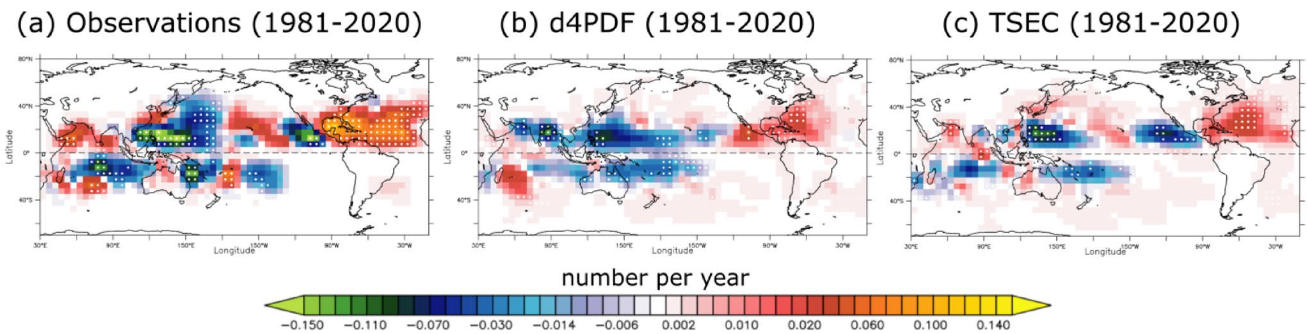

Fig. 12 Linear trends in TC frequency of occurrence for the period 1981–2020 [number per year], for (**a**) IBTrACS best track data, and the mean of 12 ensemble members from (**b**) d4PDF and (**c**) TSE-C_60km. The white dots indicate grid cells where the linear trend is statistically significant at the 90% level, according to the Mann-Kendall significance test. TC positions were counted within each 2.5 × 2.5° grid box every 6 h across the global domain. The total count for each grid box was defined as the TC frequency of occurrence

the influence of CO_2 and aerosol forcings on TC trends varies by region—for example, CO_2 forcing dominates in the eastern Pacific and near Hawaii, whereas aerosol forcing dominates in the North Atlantic, with both playing roles near Japan. The d4PDF experiment appears to emphasize aerosol-induced effects more strongly, potentially underestimating trends in CO_2-sensitive regions. In contrast, TSE-C_60km captures both aerosol- and CO_2-induced signals, resulting in a spatial trend pattern that is more consistent with observations.

5.4 Intraseasonal variation

The Madden-Julian oscillation (MJO; Madden and Julian 1971, 1972) is the dominant mode of intraseasonal variability in the tropics with a period of about 30 to 70 days, characterized by the eastward propagation of a planetary-scale convectively coupled system most prominently from the Indian Ocean to the Pacific. Previous studies show that atmosphere-ocean coupled models can improve the representation of the MJO compared to the AGCM (e.g. DeMott et al. 2015; Wu et al. 2021). The better MJO simulation skill in the coupled models is attributed to the improved representation of the moistening process through the effect of convection-SST feedback due to high-frequency SST fluctuations (DeMott et al. 2015).

We examined the skill of the MJO simulation in the TSE-C_60km experiment compared to that in the d4PDF experiment. The diagnostic method used was the same as that used for d4PDF by Takahashi et al. (2022). Figure 13a-c shows the time-longitude plots of the regressions of 20–90-day filtered precipitation anomalies averaged over 15°S–15°N and 850 hPa zonal wind (U850) anomalies against MJO-filtered (20–90-day, zonal wavenumber 1–5) precipitation anomalies averaged over the tropical Indian Ocean (85–95°E, 5°S–5°N). The analysis is performed following the MJO skill metrics (Wang et al. 2020) during the boreal winter (November–March) for 1980–2018. In the observation (Fig. 13a), the precipitation and U850, which lags precipitation by 1/4 cycle, are clearly propagated from the Indian Ocean to the Pacific. For d4PDF (Fig. 13c), the MJO amplitudes are underestimated and the propagation east of the western Pacific is unclear compared to the observation. The TSE-C_60km experiment produces larger MJO amplitudes and more realistically represents the eastward propagation into the Pacific (Fig. 13b).

The performances of MJO propagation and amplitude of the models were evaluated with a Taylor diagram (Fig. 13d). This Taylor diagram was computed from the pattern correlations with observations and the ratio of standard deviations to observations, based on the time-longitude cross sections shown in Fig. 13a-c. The pattern correlation of the ensemble mean precipitation (U850) is 0.75 (0.87) in TSE-C_60km, while it is 0.64 (0.8) in d4PDF. As for the mean amplitude skill of precipitation (U850), TSE-C_60km shows 0.85 (0.78), while d4PDF shows 0.58 (0.51). These results indicate that the MJO can be reproduced much better in TSE-C_60km than in d4PDF. The improvement is especially notable in the amplitude. Our results confirm a critical role of atmosphere-ocean coupling in the GCM representation (propagation and amplitude) of the MJO.

6 Summary and discussion

The ocean data assimilation has been introduced into a fully coupled model, MRI-ESM2. By assimilating the monthly objective analysis data of ocean temperature and salinity with a relaxation time of 10 days, the atmospheric climatology on longer time scales is reproduced as well as that of the atmosphere-only model with prescribed SST. By contrast, short-term atmosphere-ocean interactions, such as the time lag between SST and precipitation and the SST cooling due to the passage of intense tropical cyclones, are represented similarly to the fully coupled model.

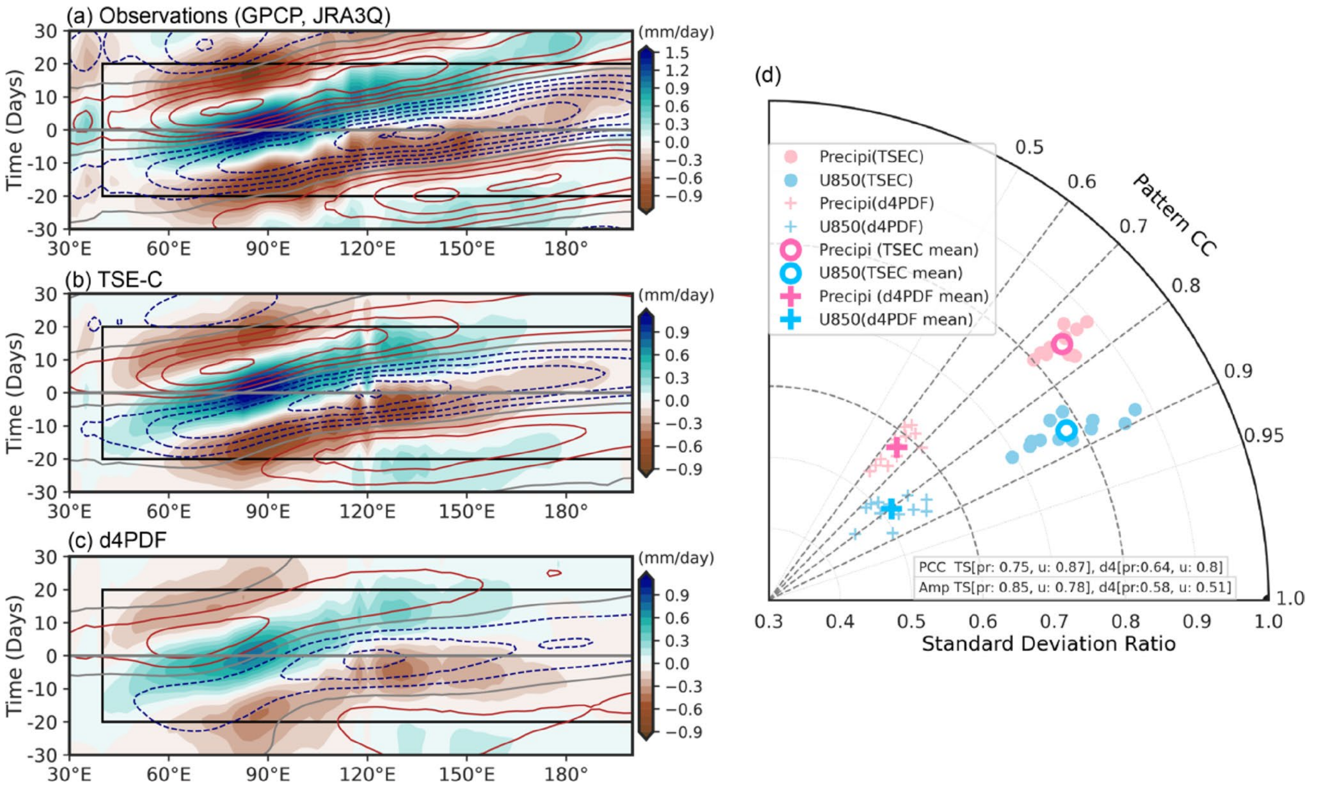

Fig. 13 (**a** - **c**) Lag-longitude diagram of intraseasonally filtered precipitation averaged over 15°S–15°N (shading) and 850 hPa zonal wind anomalies (U850, contours, 0.15 m s^{-1} interval, red: positive, blue: negative values) for (**a**) observations (GPCP and JRA-3Q), (**b**) TSE-C_60km, and (**c**) d4PDF. The diagrams are obtained as lag-regressions against MJO-filtered precipitation anomalies averaged over the tropical Indian Ocean (85–95°E, 5°S–5°N). The anomalies in (**b**) and (**c**) indicate the ensemble means (12 members). (**d**) Taylor diagram of pattern correlations and relative amplitudes for precipitation (pink) and U850 (blue) anomalies from averages over the tropical Indo-Pacific region (40–140°W, 15°S–15°N) from day −20 to +20, shown by black rectangles in (**a** - **c**). TSE-C_60km and d4PDF are marked by the circles and pluses, respectively. The thin and small (thick and large) marks represent the 12 ensemble members (ensemble means)

Simulations from the mid-20th century to the present have been performed after increasing the horizontal resolution of the atmosphere from 120 km to 60 km. The results show that the performance of the model in simulating climatological mean states on seasonal time scales is comparable to that of the previous atmosphere-only simulation, both on the global scale and in the East Asian region. The seasonal progression of the East Asian monsoon is also shown to be realistic, and the latitudinal distribution of intense tropical cyclones is improved, both of which play a very important role in the representation of extreme events over East Asia.

Although it is still difficult to represent regional extreme precipitation events in a full coupled model simulation because of the large SST error (Wehner et al. 2021), the method in this study enables us to do so while still using a coupled model. Then, if the ocean, with the changes in the CMIP model added to the observations, is used for assimilation, these changes associated with climate change can be discussed.

Therefore, we plan to update the climate simulation database of the large ensemble simulations with 60 km resolution, d4PDF, using the new system introduced in this paper. The d4PDF has been used not only for the studies of recent and future changes in extreme events associated with global warming, but also for impact assessments of natural disasters, agricultural activities and water resource management (Ishii and Mori 2020). Furthermore, based on these studies, it has been used for regional adaptation policy-making by local governments in Japan. Since the d4PDF is an atmosphere-only experiment with prescribed SST, replacing the model with the one presented in this paper would be beneficial in evaluating the influences associated with the short-term atmosphere-ocean interactions. In addition to improvements in tropical cyclones, a more realistic correlation between interannual variabilities in SST and precipitation in the western North Pacific is also represented. The atmospheric model component itself has been improved from MRI-AGCM3.2 in the d4PDF to MRI-AGCM3.5, especially in the representation of low-level clouds (Kawai et al. 2019) and stratospheric variations (Yukimoto et al. 2019). In addition, the coupled processes with the aerosol model and the atmospheric chemistry model, which were not used in the d4PDF, are also included (Table 2), allowing us to assess the impact of the recent anthropogenic aerosol trend on regional climate. We now continuously extend the time integration from the present to the end of the 21 st century. Combined with a non-warming climate simulation by removing past anthropogenic emission changes, this will allow us to investigate changes in extreme events associated with climate change from a broader perspective. Furthermore, this framework can be applied to other climate models. Increasing the resolution of atmospheric models would require modifications specific to each model, but with sufficient computing resources and data storage capacity, a larger number of ensembles can be executed accordingly. This facilitates comparisons between climate models and contributes to deepening discussions on model uncertainty regarding changes in regional climate and extreme events.

As in the d4PDF, the changes around Japan are also analyzed in more detail by a dynamical downscaling to a higher-resolution regional climate model. In the regional model, the frequency and areal extent of typhoons, and the seasonal progression of the East Asian monsoon, including their changes, are strongly dependent on the representation in the outer global model. Therefore, the improved performance in the global model will contribute to increase confidence in the results of the downscaled regional climate model simulations.

We also have a plan to use the surface atmospheric state in this global model to downscale to a regional ocean model of the western North Pacific. Using this model may provide a more realistic simulation of the Kuroshio than using the CMIP6 model output. In addition, a higher atmospheric resolution of 20 km is planned to simulate more realistic tropical cyclone intensities. By making a suite of data publicly available, we hope to be able to contribute to the formulation of global warming adaptation policies based on more realistic regional climate change projections.

Appendix A: changes made in the 60 km model

When the resolution of the atmospheric model of the TSE-C experiment was increased from 120 km to 60 km, a resolution dependence in the representation of the climate was found. The following changes have been made in the 60 km model to improve the representation of average climatic conditions, seasonal progression, tropical cyclones, etc.

- In the cloud scheme, the conversion rate of cloud ice to snow (Kawai et al. 2019) was reduced. The increase in upper clouds due to this change mitigates a resolution dependence that upper clouds become less at higher resolutions. This also mitigates the lower temperatures in the mid-upper troposphere associated with the lack of longwave radiative heating caused by the fewer upper clouds at higher resolutions.
- The time step for the calculation of longwave radiation has been reduced from 3 h to 1 h. This mitigated a resolution dependence that lower clouds are more in the tropics and less in the mid-latitudes in the higher resolution model (Kawai et al. 2019).
- The parameters for non-orographic gravity waves have been changed so that the Rayleigh friction near the top of the model does not work. Horizontal diffusion was changed to the same table as in MRI-AGCM3.2, where the coefficients are larger in the upper layers. This improved the variability of the stratospheric mean wind speed and the quasi-biennial oscillations.
- Corrections have been made to the assignment of the input solar irradiance to the model radiation bands, which was inappropriate for the CMIP6 experiments. This improved the stratospheric high temperature anomalies seen in the CMIP6 experiments.
- Changes have been made to increase the albedo over sea ice. This reduced the decreasing trend in sea ice thickness and the high temperature anomaly in the Arctic region.
- The parameters that determine the intensity of short orographic gravity waves have been changed to match the values used in the operational forecast model. This improved the underestimation of the height of 500-hPa in winter near Japan.
- Anomalous water temperatures in lakes with very small areas have been corrected by redistributing fluxes with neighboring lakes in the grid. In addition, the introduction of large lake schemes, where water and heat are distributed across the entire lake grids, has improved the simulation of lake water temperatures in large lakes such as the Caspian Sea.
- The land surface model has been modified to increase the albedo of the forest zone. This resulted in improved summer high temperature anomalies over Eurasia.
- For the ocean forcing data, the climatological values of water temperature and salinity in the Japan Sea were bias corrected with the climatological values of FORA-WNP30 (Usui et al. 2017). This improved the low temperature anomalies in the Sea of Japan in winter.

In addition to these changes, we have made changes to improve energy conservation, water mass conservation, and computational stability during long-term integration. In the following, we show the impact of the above changes on the climate representation of the East Asian summer/winter monsoon.

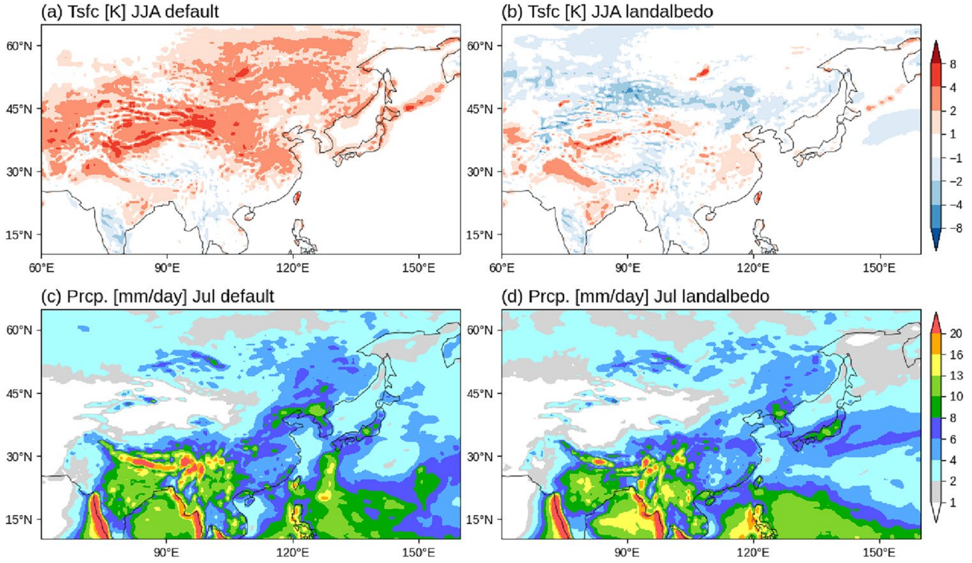

Fig. 14 (**a**, **b**) Surface air temperature anomalies from JRA-3Q during JJA and (**c**, **d**) mean precipitation during July for (**a**, **c**) the control TSE-C experiment, in which the listed changes were not included, and (**b**, **d**) the test experiment, in which the albedo of the forest zone is increased. The analysis period is 1981–1984

(a) Tsfc [K] JJA default

(b) Tsfc [K] JJA landalbedo

(c) Prcp. [mm/day] Jul default

(d) Prcp. [mm/day] Jul landalbedo

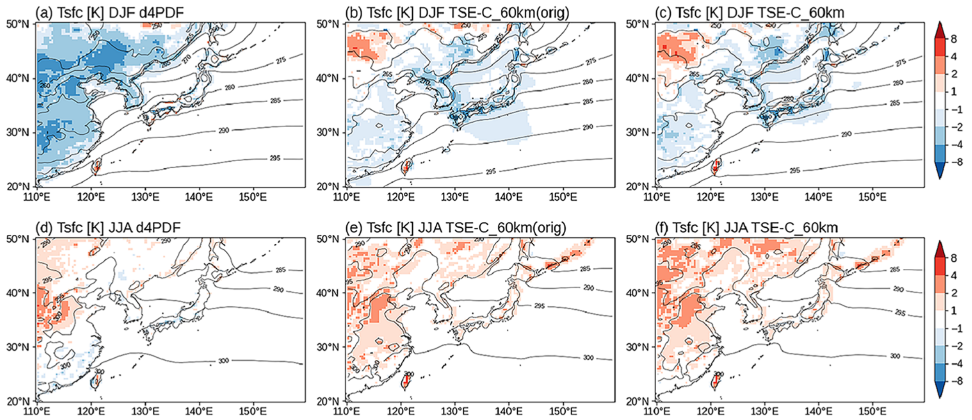

Fig. 15 Surface air temperature (contour) and its anomaly from JRA-3Q (shading) during (**a** - **c**) DJF and (**d** - **f**) JJA, for (**a**, **d**) d4PDF, (**b**, **e**) the original TSE-C experiment, in which the listed changes were not included, and (**c**, **f**) the TSE-C_60km experiments. The analysis period is 1981–2000

(a) Tsfc [K] DJF d4PDF

(b) Tsfc [K] DJF TSE-C_60km(orig)

(c) Tsfc [K] DJF TSE-C_60km

(d) Tsfc [K] JJA d4PDF

(e) Tsfc [K] JJA TSE-C_60km(orig)

(f) Tsfc [K] JJA TSE-C_60km

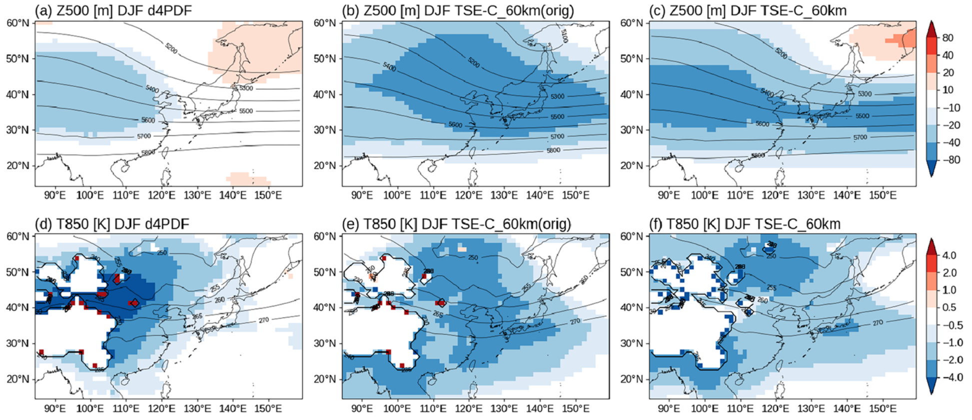

Fig. 16 Same as Fig. 15, but for (**a** - **c**) geopotential height at 500 hPa and (**d** - **f**) air temperature at 850 hPa

(a) Z500 [m] DJF d4PDF

(b) Z500 [m] DJF TSE-C_60km(orig)

(c) Z500 [m] DJF TSE-C_60km

(d) T850 [K] DJF d4PDF

(e) T850 [K] DJF TSE-C_60km(orig)

(f) T850 [K] DJF TSE-C_60km

Figure 14 shows the change in a sensitivity experiment of changing the albedo of the forest zone. As shown in Fig. 9, the Meiyu-Baiu rain band exists from southern China to southern Japan in June and July. However, the seasonal progression was earlier than that observed in the control experiment, which did not include the above changes, and the rain band disappeared in early July (Fig. 14c). The surface air temperature anomaly (Fig. 14a) is widely high over the continental Northern Hemisphere in summer, suggesting that the seasonal progression of land temperature is earlier. In the test experiment, in which the albedo of the forest zone is increased, the summer temperature over land becomes lower (Fig. 14b), and the representation of the rain band is also improved (Fig. 14d).

Figure 15 compares the seasonal mean surface air temperature anomalies from the reanalysis data around Japan. Over land in Japan, the d4PDF experiment showed temperature anomalies from the reanalysis within about 1 K in both winter and summer (Fig. 15a, d), while the original TSE-C experiment, which did not include the above changes, showed small temperature anomalies in summer but −1 to −2 K in winter (Fig. 15b, e). Such temperature anomalies could propagate to dynamical downscaling with regional climate models and have a significant impact on snowfall estimates, as the rain/snow determination of precipitation is sensitive to small temperature differences.

Four possible causes for the low temperature anomaly compared to d4PDF were considered. (1) The observed monthly mean SST is given as a boundary condition in d4PDF, resulting in a very small temperature anomaly over the ocean, while in the TSE-C the sea surface is cooled by the northwest winds of the winter monsoon. (2) The surface wind anomalies are particularly westerly in winter, which is associated with an underestimation of the 500-hPa height over Japan (Fig. 16b), i.e., an overestimation of the trough depth and a strong inflow of cold air. (3) Although the low temperature anomaly from China to Siberia is smaller in the TSE-C than in d4PDF, low temperature anomalies are still seen in the lower to middle troposphere (Fig. 16e), and these anomalies are advected by northwest winds near Japan. (4) Because the ocean forcing data are objective analysis data on a 1° grid, the accuracy is not sufficient, and low temperature anomalies are seen in the Sea of Japan.

Therefore, changes were made to mitigate the anomalies of (2), (3), and (4). For (2), the orographic gravity wave parameters were modified to be closer to the values used in the Japan Meteorological Agency (JMA) operational weather forecast model, since MRI-AGCM is derived from the JMA operational model. Figure 16 (a-c) shows the geopotential height anomaly from the reanalysis data at 500 hPa. The depth of the trough, which is deeper than in d4PDF, was reduced in the TSE-C_60km experiment, which means that the westerly wind anomaly was also reduced. For (3), a change was made to reduce the conversion rate of cloud ice to snow. This has the effect of increasing cloud cover in the mid-latitude troposphere and reducing the low-temperature anomalies there, and reduces the horizontal resolution dependence of the model, where higher resolution tends to reduce cloud cover. Figure 16 (d-f) shows 850-hPa temperature anomalies from the reanalysis data. The original experiment has a lower temperature anomaly than d4PDF from the east coast of China to Japan, but it has been reduced in the TSE-C_60km experiment mainly due to this change (Fig. 16f). For (4), the climatological values of water temperature and salinity in the Sea of Japan were bias-corrected with the climatological values from FORA-WNP30 (Usui et al. 2017). These changes reduced the winter temperature anomalies in the TSE-C_60km experiment (Fig. 15c) compared with the original TSE-C experiment, without significantly affecting the summer temperatures (Fig. 15f).

Supplementary Information The online version contains supplementary material available at https://doi.org/10.1007/s44394-025-00011-2.

Acknowledgements The calculations were performed on the Earth Simulator of the Japan Agency for Marine-Earth Science and Technology (JAMSTEC). This work was supported by MEXT program for the advanced studies of climate change projection (SENTAN) Grant Number JPMXD0722680734, and the Japan Society for the Promotion of Science (JSPS) KAKENHI grants JP21K03670. We thank two reviewers for their insightful comments that helped to improve this manuscript.

Author contributions M.I. introduced the ocean assimilation process. R.M., H.K., S.Y., K.Y., H.Y., H.T., Y.U., and H.E. tested and improved the model performance. R.M., K.Y., and Y.U. performed the numerical simulations. H.E., T.M., R.M., H.M., and C.T. prepared figures. R.M., H.E., H.M., and C.T. wrote the main manuscript text. All authors reviewed the manuscript.

Data availability The results of model experiments using MRI-ESM2 are available at https://climate.mri-jma.go.jp/pub/archives/Mizuta-et-al_TSE-C/. The description of MRI-ESM2 is provided by Yukimoto et al. (2019). The source code of MRI-ESM2 is the property of Meteorological Research Institute (MRI)/Japan Meteorological Agency, and is not open source, but is available under a collaborative framework with MRI. The d4PDF and JRA-3Q reanalysis data are available at the Data Integration and Analysis System (DIAS) website (http://search.diasjp.net/en/dataset/d4PDF_GCM, and https://search.diasjp.net/en/dataset/JRA3Q). The monthly objective analysis of ocean temperature and salinity used for the ocean data assimilation (Ishii et al. 2017) and COBE-SST2 sea surface temperature and sea ice concentration data (Hirahara et al. 2014) are available at https://climate.mri-jma.go.jp/pub/ocean/ts/and https://climate.mri-jma.go.jp/pub/ocean/cobe-sst2/. GPCP, CMAP, and IMERG precipitation data are available at https://www.ncei.noaa.gov/data/, https://psl.noaa.gov/data/gridded/data.cmap.html, and https://gpm.nasa.gov/data/imerg, respectively. ERA5 reanalysis data is available from the Copernicus Climate Change Service (C3S) Climate Data Store (CDS) (Hersbach et al. 2023). IBTrACS tropical cyclone data is obtained from https://www.ncei.noaa.gov/products/international-best-track-archive. CMIP6 model results are available at the Program for Climate Model Diagnosis and Intercomparison (PCMDI); https://pcmdi.llnl.gov/CMIP6/.

Declarations

Competing interests The authors have no relevant financial or non-financial interests to disclose. The authors have no competing interests to declare that are relevant to the content of this article. All authors certify that they have no affiliations with or involvement in any organization or entity with any financial interest or non-financial interest in the subject matter or materials discussed in this manuscript. The authors have no financial or proprietary interests in any material discussed in this article.

References

Adler RF, Huffman GJ, Chang A, Ferraro R, Xie P, Janowiak J, Rudolf B, Schneider U, Curtis S, Bolvin D, Gruber A, Susskind J, Arkin P (2003) The version 2 Global Precipitation Climatology Project (GPCP) monthly precipitation analysis (1979–present). J Hydrometeorol 4:1147–1167. https://doi.org/10.1175/1525-7541(2003)004%3C1147:TVGPCP%3E2.0.CO;2

Arakawa O, Kitoh A (2004) Comparison of local precipitation–SST relationship between the observation and a reanalysis dataset. Geophys Res Lett 31:L12206. https://doi.org/10.1029/2004GL020283

Bloom SC, Takacs LL, Da Silva AM, Ledvina D (1996) Data assimilation using incremental analysis updates. Mon Weather Rev 124:1256–1271. https://doi.org/10.1175/1520-0493(1996)124%3C1256:DAUIAU%3E2.0.CO;2

Chen T-C, Wang S-Y, Huang W-R, Yen M-C (2004) Variation of the East Asian summer monsoon rainfall. J Clim 17:744–762. https://doi.org/10.1175/1520-0442(2004)017%3C0744:VOTEAS%3E2.0.CO;2

Chiang JCH, Kong WW, Wu CH, Battisti DS (2020) Origins of East Asian summer monsoon seasonality. J Clim 33:7945–7965. https://doi.org/10.1175/JCLI-D-19-0888.1

DeMott CA, Klingaman NP, Woolnough SJ (2015) Atmosphere–ocean coupled processes in the Madden-Julian Oscillation. Rev Geophys 53:1099–1154. https://doi.org/10.1002/2014RG000478

Deushi M, Shibata K (2011) Development of a meteorological research Institute Chemistry-Climate model version 2 for the study of tropospheric and stratospheric chemistry. Pap Meteorol Geophys 62:1–46. https://doi.org/10.2467/mripapers.62.1

Ding Y (2007) The variability of the Asian summer monsoon. J Meteorol Soc Japan 85B:21–54. https://doi.org/10.2151/jmsj.85B.21

Endo H, Kitoh A, Ose T, Mizuta R, Kusunoki S (2012) Future changes in Asian precipitation simulated by multi-physics and multi-sea surface temperature ensemble experiments with high-resolution Meteorological Research Institute atmospheric general circulation models (MRI-AGCMs). J Geophys Res 117:D16118. https://doi.org/10.1029/2012JD017874

Eyring V, Bony S, Meehl GA, Senior CA, Stevens B, Stouffer RJ, Taylor KE (2016) Overview of the coupled model intercomparison project phase 6 (CMIP6) experimental design and organization. Geosci Model Dev 9(5):1937–1958. https://doi.org/10.5194/gmd-9-1937-2016

Fujita M, Mizuta R, Ishii M, Endo H, Sato T, Okada Y, Kawazoe S, Sugimoto S, Ishihara K, Watanabe S (2019) Precipitation changes in a climate with 2-K surface warming from large ensemble simulations using 60-km global and 20-km regional atmospheric models. Geophys Res Lett 46:435–442. https://doi.org/10.1029/2018GL079885

Haarsma RJ, Roberts M, Vidale PL, Senior CA, Bellucci A, Bao Q, Chang P, Corti S, Fučkar NS, Guemas V, von Hardenberg J, Hazeleger W, Kodama C, Koenigk T, Leung L-YR, Lu J, Luo J-J, Mao J, Mizielinski MS, Mizuta R, Nobre P, Satoh M, Scoccimarro E, Semmler T, Small J, von Storch J-S (2016) High resolution model intercomparison project (HighResMIP v1.0) for CMIP6. Geosci Model Dev 9:4185–4208. https://doi.org/10.5194/gmd-9-4185-2016

Hersbach H, Bell B, Berrisford P, Biavati G, Horányi A, Muñoz Sabater J, Nicolas J, Peubey C, Radu R, Rozum I, Schepers D, Simmons A, Soci C, Dee D, Thépaut J-N (2023) ERA5 monthly averaged data on pressure levels from 1940 to present. https://doi.org/10.24381/cds.6860a573. Copernicus Climate Change Service (C3S) Climate Data Store (CDS)

Hines CO (1997) Doppler-spread parameterization of gravity-wave momentum deposition in the middle atmosphere. Part 2: broad and quasi monochromatic spectra, and implementation. J Atmos Solar Terr Phys 59:387–400. https://doi.org/10.1016/S1364-6826(96)00080-6

Hirahara S, Ishii M, Fukuda Y (2014) Centennial-scale sea surface temperature analysis and its uncertainty. J Clim 27(1):57–75. https://doi.org/10.1175/JCLI-D-12-00837.1

Hirai M, Sakashita T, Kitagawa H, Tsuyuki T, Hosaka M, Oh'izumi M (2007) Development and validation of a new land surface model for JMA's operational global model using the CEOP observation dataset. J Meteorol Soc Jpn 85A:1–24. https://doi.org/10.2151/jmsj.85A.1

Huang B, Kinter JL, Schopf PS (2002) Ocean data assimilation using intermittent analyses and continuous model error correction. Adv Atmos Sci 19:965–992. https://doi.org/10.1007/s00376-002-0059-z

Huffman GJ (2020) Integrated Multi-satellite Retrievals for the Global Precipitation Measurement (GPM) Mission (IMERG). In: Levizzani V, Kidd C, Kirschbaum DB, Kummerow CD, Nakamura K, Turk FJ (eds) Satellite Precipitation Measurement. Advances in Global Change Research 67. Springer, Cham. https://doi.org/10.1007/978-3-030-24568-9_19

Huffman GJ, Adler RF, Morrissey MM, Bolvin DT, Curtis S, Joyce R, McGavock B, Susskind J (2001) Global precipitation at one-degree daily resolution from multi-satellite observations. J Hydrometeorol 2:36–50. https://doi.org/10.1175/1525-7541(2001)002%3C0036:GPAODD%3E2.0.CO;2

Imada Y, Kawase H, Watanabe M, Arai M, Shiogama H, Takayabu I (2020) Advanced risk-based event attribution for heavy regional rainfall events. NPJ Clim Atmos Sci 3:37. https://doi.org/10.1038/s41612-020-00141-y

Intergovernmental Panel on Climate Change (IPCC) (2021) Summary for policymakers. In: Masson-Delmotte V et al (eds) Climate change 2021: the physical science basis. Cambridge University Press 3–32

Ishii M, Fukuda Y, Hirahara S, Yasui S, Suzuki T, Sato K (2017) Accuracy of global upper ocean heat content estimation expected from present observational data sets. SOLA 13:163–167. https://doi.org/10.2151/sola.2017-030

Ishii M, Mori N (2020) D4PDF: large-ensemble and high-resolution climate simulations for global warming risk assessment. Prog Earth Planet Sci. https://doi.org/10.1186/s40645-020-00367-7

Ishii M, Nishimura A, Yasui S, Hirahara S (2025) Historical high-resolution daily SST analysis (COBE-SST3) with consistency to monthly land surface air temperature. J Meteorol Soc Jpn 103:17–44. https://doi.org/10.2151/jmsj.2025-002

Iwasaki T, Yamada S, Tada K (1989) A parameterization scheme of orographic gravity wave drag with two different vertical partitionings. Part I: impacts on medium-range forecasts. J Meteorol Soc Jpn 67:11–27. https://doi.org/10.2151/jmsj1965.67.1_11

Japan Meteorological Agency (2007) Outline of the operational numerical weather prediction at the Japan meteorological agency March 2007 (Appendix to WMO numerical weather prediction progress report on the global data-processing and forecasting system and numerical weather prediction research). Japan Meteorological Agency, 194pp. http://www.jma.go.jp/jma/jma-eng/jma-center/nwp/outline2007-nwp/index.htm

Kawai H, Yukimoto S, Koshiro T, Oshima N, Tanaka T, Yoshimura H, Nagasawa R (2019) Significant improvement of cloud representation in global climate model MRI-ESM2. Geosci Model Dev 12:2875–2897. https://doi.org/10.5194/gmd-12-2875-2019

Kawase H, Murata A, Mizuta R, Sasaki H, Nosaka M, Takayabu I (2016) Enhancement of extreme daily snowfall in Japan due to global warming projected by enormous ensemble regional climate experiments. Clim Change 139:265–278. https://doi.org/10.1007/s10584-016-1781-3

Kawase H, Murata A, Yamada K, Nakaegawa T, Ito R, Mizuta R, Nosaka M, Watanabe S, Sasaki H (2021) Regional characteristics of future changes in snowfall in Japan under RCP2.6 and RCP8.5 scenarios. SOLA 17:1–7. https://doi.org/10.2151/sola.2021-001

Kennedy J, Titchner H, Rayner N, Roberts M (2017) input4MIPs. MOHC. SSTsAndSeaIce. HighResMIP. MOHC-HadISST-2-2-0-0-0. https://doi.org/10.22033/ESGF/input4MIPs.1221. Earth System Grid Federation

Kitoh A, Ose T, Takayabu I (2016) Dynamical downscaling for climate projection with high-resolution MRI AGCM-RCM. J Meteor Soc Japan 94A:1–16. https://doi.org/10.2151/jmsj.2015-022

Knapp KR, Kruk MC, Levinson DH, Diamond HJ, Neumann CJ (2010) The international best track archive for climate stewardship (IBTrACS): unifying tropical cyclone best track data. Bull Am Meteor Soc 91:363–376. https://doi.org/10.1175/2009BAMS2755.1

Kosaka Y, Kobayashi S, Harada Y, Kobayashi C, Naoe H, Yoshimoto K, Harada M, Goto N, Chiba J, Miyaoka K, Sekiguchi R, Deushi M, Kamahori H, Nakaegawa T, Tanaka TY, Tokuhiro T, Sato Y, Matsushita Y, Onogi K (2024) The JRA-3Q reanalysis. J Meteorol Soc Japan Ser II 102:49–109. https://doi.org/10.2151/jmsj.2024-004

Kumar A, Chen M, Wang W (2013) Understanding prediction skill of seasonal mean precipitation over the tropics. J Clim 26:5674–5681. https://doi.org/10.1175/JCLI-D-12-00731.1

Kusunoki S (2018) Future changes in precipitation over East Asia projected by the global atmospheric model MRI-AGCM3.2. Clim Dyn 51:4601–4617. https://doi.org/10.1007/s00382-016-3499-3

Levitus S, Boyer TP, Garcia HE, Locarnini RA, Zweng MM, Mishonov AV, Reagan JR, Antonov JI, Baranova OK, Biddle M, Hamilton M, Johnson DR, Paver CR, Seidov D (2015) World ocean atlas 2013 (NCEI accession 0114815). NOAA Natl Centers Environ Inform. https://doi.org/10.7289/v5f769gt

Madden AA, Julian PR (1971) Detection of a 40–50 day oscillation in the zonal wind in the tropical Pacific. J Atmos Sci 28:702–708. https://doi.org/10.1175/1520-0469(1971)028%3C0702:DOADOI%3E2.0.CO;2

Madden AA, Julian PR (1972) Description of global-scale circulation cells in the tropics with a 40–50 day period. J Atmos Sci 29:1109–1123. https://doi.org/10.1175/1520-0469(1972)029%3C1109:DOGSCC%3E2.0.CO;2

Mellor GL, Yamada T (1974) A hierarchy of turbulence closure models for planetary boundary layers. J Atmos Sci 31:1791–1806. https://doi.org/10.1175/1520-0469(1974)031

Mellor GL, Yamada T (1982) Development of a turbulence closure model for geophysical fluid problems. Rev Geophys Space Phys 20:851–875. https://doi.org/10.1029/RG020i004p00851

Mizuta R, Murata A, Ishii M, Shiogama H, Hibino K, Mori N, Arakawa O, Imada Y, Yoshida K, Aoyagi T, Kawase H, Mori M, Okada Y, Shimura T, Nagatomo T, Ikeda M, Endo H, Nosaka M, Arai M, Takahashi C, Tanaka K, Takemi T, Tachikawa Y, Temur K, Kamae Y, Watanabe M, Sasaki H, Kitoh A, Takayabu I, Nakakita E, Kimoto M (2017) Over 5000 years of ensemble future climate simulations by 60 Km global and 20 Km regional atmospheric models. Bull Am Meteorol Soc 98:1383–1398. https://doi.org/10.1175/BAMS-D-16-0099.1

Mizuta R, Nosaka M, Nakaegawa T, Endo H, Kusunoki S, Murata A, Takayabu I (2022) Extreme precipitation in 150-year continuous simulations by 20-km and 60-km atmospheric general circulation models with dynamical downscaling over Japan by a 20-km regional climate model. J Meteorol Soc Japan 100:523–532. https://doi.org/10.2151/jmsj.2022-026

Mizuta R, Yoshimura H, Murakami H, Matsueda M, Endo H, Ose T, Kamiguchi K, Hosaka M, Sugi M, Yukimoto S, Kusunoki S, Kitoh A (2012) Climate simulations using MRI-AGCM3.2 with 20-km grid. J Meteorol Soc Japan 90A:233–258. https://doi.org/10.2151/jmsj.2012-A12

Murakami H, Delworth TL, Cooke WF, Zhao M, Xiang B, Hsu P-C (2020) Detected climatic change in global distribution of tropical cyclones. Proc Natl Acad Sci U S A 117(20):10706–10714. https://doi.org/10.1073/pnas.1922500117

Murakami H, Delworth TL, Johnson NC, Lu F, McHugh CE, Jia L (2025) Seasonal forecasts of tropical cyclones using GFDL SPEAR and HiFLOR-S. J Clim 38:2015–2030. https://doi.org/10.1175/JCLI-D-24-0356.1

Murakami H, Wang Y, Yoshimura H, Mizuta R, Sugi M, Shindo E, Adachi Y, Yukimoto S, Hosaka M, Kusunoki S, Ose T, Kitoh A (2012) Future changes in tropical cyclone activity projected by the new high-resolution MRI-AGCM. J Clim 25:3237–3260. https://doi.org/10.1175/JCLI-D-11-00415.1

Nakanishi M (2001) Improvement of the Mellor-Yamada turbulence closure model based on large-eddy simulation data. Boundary-Layer Meteorol 99:349–378. https://doi.org/10.1023/A:1018915827400

Nakanishi M, Niino H (2004) An improved Mellor-Yamada level-3 model with condensation physics: its design and verification. Boundary-Layer Meteorol 112:1–31. https://doi.org/10.1023/B:BOUN.0000020164.04146.98

Nosaka M, Ishii M, Shiogama H, Mizuta R, Murata A, Kawase H, Sasaki H (2020) Scalability of future climate changes across Japan examined with large-ensemble simulations at +1.5 K, +2 K, and +4 K global warming levels. Prog Earth Planet Sci. https://doi.org/10.1186/s40645-020-00341-3

Ogata T, Mizuta R, Adachi Y, Murakami H, Ose T (2015) Effect of air-sea coupling on the frequency distribution of intense tropical cyclones over the northwestern Pacific. Geophys Res Lett 42:10415–10421. https://doi.org/10.1002/2015GL066774

Price JF (2009) Metrics of hurricane-ocean interaction: vertically-integrated or vertically-averaged ocean temperature? Ocean Sci 5:351–368. https://doi.org/10.5194/os-5-351-2009

Reynolds RW, Chelton DB (2010) Comparisons of daily sea surface temperature analyses for 2007–08. J Clim 23:3545–3562. https://doi.org/10.1175/2010JCLI3294.1

Roberts MJ, Camp J, Seddon J, Vidale PL, Hodges K, Vannière B, Mecking J, Haarsma R, Bellucci A, Scoccimarro E, Caron L-P, Chauvin F, Terray L, Valcke S, Moine M-P, Putrasahan D, Roberts CD, Senan R, Zarzycki C, Ullrich P, Yamada Y, Mizuta R, Kodama C, Fu D, Zhang Q, Danabasoglu G, Rosenbloom N, Wang H, Wu L (2020) Projected future changes in tropical cyclones using the CMIP6 HighResMIP multimodel ensemble. Geophys Res Lett 47:e2020GL088662. https://doi.org/10.1029/2020GL088662

Sampe T, Xie S-P (2010) Large-scale dynamics of the Meiyu-Baiu rainband: environmental forcing by the Westerly jet. J Clim 23:113–134. https://doi.org/10.1175/2009JCLI3128.1

Si W, Liu H, Zhang X, Zhang M (2021) Double Intertropical convergence zones in coupled Ocean-Atmosphere models: progress in CMIP6. Geophys Res Lett 48. https://doi.org/10.1029/2021GL094

Song F, Zhou T (2014) The climatology and interannual variability of East Asian summer monsoon in CMIP5 coupled models: Does air-sea coupling improve the simulations? J Climate 27:8761-8777. https://doi.org/10.1175/JCLI-D-14-00396.1

Stott PA (2016) Attribution of extreme weather and climate-related events. Wiley Interdiscip Rev Clim Change 7:23–41. https://doi.org/10.1002/wcc.380

Takahashi C, Imada Y, Watanabe M (2022) Influence of the Madden–Julian oscillation on wintertime extreme snowfall and precipitation in Japan. J Meteorol Soc Japan 100:257–283. https://doi.org/10.2151/jmsj.2022-014

Tanaka TY, Ogi A (2017) Update of Japan meteorological agency's global mineral dust operational forecast model. Sokkō-Jihō 84:109–128

Tanaka TY, Orito K, Sekiyama TT, Shibata K, Chiba M, Tanaka H (2003) MASINGAR, a global tropospheric aerosol chemical transport model coupled with MRI/JMA98 GCM: model description. Pap Meteorol Geophys 53:119–138. https://doi.org/10.2467/mripapers.53.119

Tatebe H, Ishii M, Mochizuki T, Chikamoto Y, Sakamoto TT, Komuro Y, Mori M, Yasunaka S, Watanabe M, Ogochi K, Suzuki T, Nishimura T, Kimoto M (2012) The initialization of the MIROC climate models for decadal prediction with hydrographic data assimilation. J Meteorol Soc Japan 90A:275–294. https://doi.org/10.2151/jmsj.2012-A14

Taylor KE (2001) Summarizing multiple aspects of model performance in a single diagram. J Geophys Res 106:7183–7192. https://doi.org/10.1029/2000JD900719

Tian B, Dong X (2020) The double-ITCZ bias in CMIP3, CMIP5, and CMIP6 models based on annual mean precipitation. Geophys Res Lett. https://doi.org/10.1029/2020GL087232

Tiedtke M (1993) Representation of clouds in large-scale models. Mon Weather Rev 121:3040–3061. https://doi.org/10.1175/1520-0493(1993)121

Tsujino H, Nakano H, Sakamoto K, Urakawa S, Hirabara M, Ishizaki H, Yamanaka G (2017) Reference manual for the meteorological research Institute community ocean model version 4 (MRI.COMv4). Tech Rep Meteorol Res Inst 80:306. https://doi.org/10.11483/mritechrepo.80

Usui N, Wakamatsu T, Tanaka Y, Hirose N, Toyoda T, Nishikawa S, Fujii Y, Takatsuki Y, Igarashi H, Nishikawa H, Ishikawa Y, Kuragano T, Kamachi M (2017) Four-dimensional variational ocean reanalysis: a 30-year high-resolution dataset in the Western North Pacific (FORA-WNP30). J Oceanogr 73:205–233. https://doi.org/10.1007/s10872-016-0398-5

Vecchi GA, Delworth T, Murakami H, Underwood S, Wittenberg AT, Zeng F, Zhang W, Baldwin JW, Bhatia K, Cooke W, He J, Kapnick SB, Knutson T, Villarini G, van der Wiel K, Anderson W, Balaji V, Chen J, Dixon K, Gudgel R, Harris L, Jia L, Johnson N, Lin S, Liu M, Ng J, Rosati A, Smith J, Yang X (2019) Tropical cyclone sensitivities to CO2 doubling: roles of atmospheric resolution, synoptic variability and background climate changes. Clim Dyn 53(9–10):5999–6033. https://doi.org/10.1007/s00382-019-04913-y

Vincent EM, Lengaigne M, Vialard J, Madec G, Jourdain NC, Masson S (2012) Assessing the oceanic control on the amplitude of sea surface cooling induced by tropical cyclones. J Geophys Res 117:C05023. https://doi.org/10.1029/2011JC007705

Wang B, Ding Q, Fu X, Kang I-S, Jin K, Shukla J, Doblas-Reyes F (2005) Fundamental challenge in simulation and prediction of summer monsoon rainfall. Geophys Res Lett 32:L15711. https://doi.org/10.1029/2005GL022734

Wang B, Wu Z, Li J, Liu J, Chang C-P, Ding Y, Wu G (2008) How to measure the strength of the East Asian summer monsoon. J Clim 21:4449–4463. https://doi.org/10.1175/2008JCLI2183.1

Wang J, Kim H, Henderson SA, Stan C, Maloney ED (2020) MJO teleconnections over the PNA region in climate models. Part II: impacts of the MJO and basic state. J Clim 33:5081–5101. https://doi.org/10.1175/JCLI-D-19-0865.1

Wang S, Murakami H, Cooke WF (2023) Anthropogenic forcing changes coastal tropical cyclone frequency. Npj Clim Atmos Sci 6:187. https://doi.org/10.1038/s41612-023-00516-x

Wehner M, Lee J, Risser M, Ullrich P, Gleckler P, Collins WD (2021) Evaluation of extreme sub-daily precipitation in high-resolution global climate model simulations. Philos Trans R Soc Lond A Math Phys Eng Sci 379:20190545. https://doi.org/10.1098/rsta.2019.0545

Woolnough SJ, Slingo JM, Hoskins BJ (2000) The relationship between convection and sea surface temperature on intraseasonal timescales. J Climate 13:2086–2104. https://doi.org/10.1175/1520-0442(2000)013%3C2086:TRBCAS%3E2.0.CO;2

Wu J, Li Y, Luo J-J, Jiang X (2021) Assessing the role of air–sea coupling in predicting Madden–Julian Oscillation with an atmosphere–ocean coupled model. J Clim 34:9647–9663. https://doi.org/10.1175/JCLI-D-20-0989.1

Xie P, Adler RF, Huffman GJ, Bolvin D (2011) Global precipitation climatology Project - Pentad, version 2.2. NOAA National Climatic Data Center

Xie P, Arkin PA (1997) Global precipitation: a 17-year monthly analysis based on gauge observations, satellite estimates and numerical model outputs. Bull Am Meteorol Soc 78:2539–2558. https://doi.org/10.1175/1520-0477(1997)078%3C2539:GPAYMA%3E2.0.CO;2

Yoshida K, Sugi M, Mizuta R, Murakami H, Ishii M (2017) Future changes in tropical cyclone activity in high-resolution large-ensemble simulations. Geophys Res Lett 44:9910–9917. https://doi.org/10.1002/2017GL075058

Yoshimura H, Mizuta R, Murakami H (2015) A spectral cumulus parameterization scheme interpolating between two convective updrafts with semi-lagrangian calculation of transport by compensatory subsidence. Mon Weather Rev 143:597–621. https://doi.org/10.1175/MWR-D-14-00068.1

Yukimoto S, Kawai H, Koshiro T, Oshima N, Yoshida K, Urakawa S, Tsujino H, Deushi M, Tanaka T, Hosaka M, Yabu S, Yoshimura H, Shindo E, Mizuta R, Obata A, Adachi Y, Ishii M (2019) The meteorological research Institute Earth system model version 2.0, MRI-ESM2.0: description and basic evaluation of the physical component. J Meteorol Soc Japan 97:931–965. https://doi.org/10.2151/jmsj.2019-051

Yukimoto S, Yoshimura H, Hosaka M, Sakami T, Tsujino H, Hirabara M, Tanaka TY, Deushi M, Obata A, Nakano H, Adachi Y, Shindo E, Yabu S, Ose T, Kitoh A (2011) Meteorological Research Institute–Earth System Model version 1 (MRI-ESM1): Model description. Technical Reports of the Meteorological Research Institute, 64, 88 pp. https://doi.org/10.11483/mritechrepo.64

Zhou Z, Xie S, Zhang GJ, Zhou W (2018) Evaluating AMIP skill in simulating interannual variability over the Indo–Western Pacific. J Clim 31(6):2253–2265. https://doi.org/10.1175/JCLI-D-17-0123.1